The synergy of morphology and mixing state on the absorption of coated black carbon soot

Johannes Heuser[1,2,a],*, Claudia Di Biagio[2,*] Jérôme Yon[3], Mathieu Cazaunau[1], Antonin Bergé[2,b], Edouard Pangui[1], Marco Zanatta[1,4], Laura Renzi[4], Angela Marinoni[4], Chenjie Yu[2], Servanne Chevaillier[1], Daniel Ferry[5], Paolo Laj[6,c], Michel Maillé[1], Paola Formenti[2], Benedicte Picquet-Varrault[1], and Jean-Francois Doussin[1]

[1] Univ Paris Est Creteil and Université Paris Cité, CNRS, LISA, F-94010 Créteil, France
[2] Université Paris Cité and Univ Paris Est Creteil, CNRS, LISA, F-75013 Paris, France
[3] INSA Rouen Normandie, Univ. Rouen Normandie, CNRS, Normandie Univ., CORIA UMR 6614, 76000, Rouen France
[4] Institute of Atmospheric Sciences and Climate, National Research Council of Italy, Bologna, Italy
[5] Aix Marseille Univ., CNRS, CINaM, Marseille, France
[6] Univ. Grenoble Alpes, IRD, CNRS, INRAE, Grenoble INP, IGE, 38000 Grenoble, France
[a] now at : Deutscher Wetterdienst, Frahmredder 95, D-22393 Hamburg, Germany
[b] now at : Laboratoire des Sciences du Climat et de l'Environnement, CEA–CNRS–UVSQ, IPSL, Université Paris-Saclay, 91191 Gif-sur-Yvette, France
[c] now at: World Meteorological Organization, Geneva, Switzerland

*Corresponding author. Email: Johannes Heuser (hannes.heu@gmail.com) & Claudia Di Biagio (claudia.dibiagio@lisa.ipsl.fr)

Abstract

Black carbon (BC) strongly absorbs light and contributes to climate warming. Coating formation on fractal BC-containing soot is a ubiquitous atmospheric process that enhances its absorption, but the extent of this absorption enhancement (E_{abs}) remains uncertain and difficult to represent in models. In this study, we use large simulation chamber experiments to investigate BC absorption and its modification by coating formation and ageing. Polydisperse fractal BC-containing soot was mixed with non-absorbing atmospherically-relevant secondary aerosols (sulfuric acid and α-pinene secondary organic aerosols). Varying reaction dynamics produced different coating rates and masses, mimicking atmospheric processing. The evolution of soot and coating properties was tracked for up to 20 hours. The results of this study suggest a general positive correlation between E_{abs} and coating amount on soot. However, they also experimentally demonstrate the strong effect of morphological modifications and mixing state heterogeneity on BC absorption, both depending on the reaction dynamics of coating formation and ageing of the coated soot. Combined variations in morphology and mixing state affect the magnitude of E_{abs} and its further evolution, leading, depending on processing, to either an increase or decrease in absorption. The range of measured E_{abs} resulting from soot processing cannot be reliably represented using a fixed E_{abs} value or by a core-shell optical model, two approximations commonly used in climate models. These results support the need for new formalisms that would take into account both morphological and mixing state heterogeneity to improve model predictions of BC absorption and its role on the radiative budget.

1 Introduction

Black carbon (BC) is the major aerosol light-absorber and one of the strongest contributors to modern climate forcing (Bond et al., 2013; Intergovernmental Panel on Climate Change (IPCC), 2023; Lee et al., 2021). Soot, as the most common BC-containing aerosol, is emitted as a product of incomplete combustion of biomass, biofuels, and fossil fuels, and displays a broad atmospheric distribution ranging from the surface into the stratosphere and from urban environments to remote locations (Bond et al., 2013; Liu et al., 2020; Schwarz et al., 2006). Light absorption by BC in soot is strongly affected by internal mixing with brown carbon (Cheng et al., 2019; Heuser et al., 2025) and secondary species (Colbeck et al., 1990; Schnaiter et al., 2005; Wang et al., 2017; Zhang et al., 2018), either co-emitted or formed during atmospheric lifetime. In particular, the formation of a non- or weakly-absorbing coating on soot has been established to enhance its absorption due to refracting and reflecting effects (Bond and Bergstrom, 2006; Cappa et al., 2012, 2019; Fuller et al., 1999). This enhancement is commonly expressed via the enhancement factor E_{abs}, which is the ratio between the absorption of the coated and the uncoated soot.

Currently, the magnitude and dependencies of E_{abs} on coating and soot properties remain controversial (Cappa et al., 2012; Fierce et al., 2016, 2020; Liu et al., 2017; Peng et al., 2016). Most studies generally describe an increasing E_{abs} with an increasing coating-to-soot or coating-to-BC mass ratio. Laboratory works retrieved E_{abs} values as high as 2 for internally mixed soot with varying coating-to-BC mass ratios (Cappa et al., 2012; Lack et al., 2009; Peng et al., 2016; Schnaiter et al., 2005). Field observations led to diverse results, with some studies reporting E_{abs} up to 3 (Liu et al., 2015, 2017; Zhang et al., 2018), while others calculate small E_{abs} despite large coating masses (Cappa et al., 2012, 2019; Chan et al., 2010; Healy et al., 2015; Huang et al., 2024). The spread of observations suggests that the mechanisms leading to absorption enhancement do not depend solely on the amount of coating mass deposited on the BC. Key aspects evidenced to affect E_{abs} magnitude and variability include (i) the single particle properties and mixing state including the morphological organization of the soot and its coating (Chen et al., 2024; Huang et al., 2024; Liu et al., 2017; Sedlacek III et al., 2012), i.e. the way secondary species distributes over the fractal soot including void filling or encapsulating soot with consequent collapse of the aggregate; (ii) the diversity in the particle-to-particle mixing state in the soot population (Cappa et al., 2019; Fierce et al., 2020; Wang et al., 2023; Zeng et al., 2024), and the (iii) rate of coating formation and ageing (Cappa et al., 2019; Peng et al., 2016). Despite advances in identifying the various mechanisms contributing to the variability of soot absorption, including evaluation of instrumental and methodological uncertainties (Asmi et al., 2025), the process-level understanding of the impact of ageing on E_{abs} remains elusive.

As a consequence of this lack of knowledge, and despite the evident variability, most climate models keep an oversimplified estimation of E_{abs} either via a concentric core-shell optical model (the Mie core-shell for spherical coated particles) or a fixed E_{abs} factor, often set at the value of 1.5 (Sand et al., 2021). However, both approximations are identified to overestimate E_{abs} (Cappa et al., 2019; Fierce et al., 2020; Liu et al., 2017; Wang et al., 2023).

In order to advance towards a mechanistic understanding of E_{abs}, in this work, we investigate the absorption of BC and its modification due to coating formation based on systematic laboratory experiments in a large simulation chamber. We generated polydisperse fractal BC-containing soot and mixed it with non-absorbing atmospherically-relevant secondary aerosol species (sulfuric acid, H_2SO_4, and α-pinene secondary organic aerosols, SOA). Multiple coating experiments were performed with varying reaction dynamics, leading to slower/faster and lower/higher coating mass formation, mimicking the processing occurring in the

atmosphere. The evolution of the soot and coating properties over up to 20 hours of chamber lifetime was studied to evaluate the E_{abs} magnitude and variability, and its link to physico-chemical properties.

2 Methods

This study utilises the 4.2 m^3 stainless steel CESAM atmospheric simulation chamber (French acronym for Experimental Multiphasic Atmospheric Simulation Chamber) (Doussin et al., 2023; Wang et al., 2011) (https://cesam.cnrs.fr/, last access: 17 July 2026). CESAM is a temperature-, pressure-, and humidity-controlled chamber designed to allow multiphase atmospheric (photo-) chemistry, widely used to investigate the formation, evolution and climate-relevant properties of primary and secondary sub- and super-micron aerosols (Baldo et al., 2020, 2023; Battaglia et al., 2025; Caponi et al., 2017; De Haan et al., 2023; Di Biagio et al., 2017, 2019, 2023; Heuser et al., 2025). The gaseous and aerosol content can be varied in CESAM to reproduce atmospherically-relevant mixtures under varying particles and gas-phase concentrations. Realistic solar irradiation is provided by three 6.5 kW Xenon arc lamps. A stainless steel fan placed at the bottom of the reactor ensures the homogeneity within the volume, with a mixing time of around one minute. The aerosol lifetime in the chamber is between 6 to more than 24 hours for particles of diameter between 50 and 200 nm (Lamkaddam et al., 2017). CESAM is equipped with 12 circular flanges enabling the deployment of multiple instruments for online and offline measurements of the chamber's thermodynamic state, gas-phase composition, aerosol concentration and their physico-chemical and spectral optical properties.

A total of 16 experiments were performed to investigate the evolution of the soot optical properties due to different ageing conditions, as summarized in Table 1. Six of these experiments targeted the formation of a coating on soot under diverse reactions dynamics and its subsequent ageing. In three experiments, H_2SO_4 coating was generated via the reaction of SO_2 and hydroxyl radical (OH). In two of these experiments (H_2SO_4-high1, H_2SO_4-high2), O_3 (at concentration of about 950 ppb) was used for OH-radical production via photolysis in the presence of water vapour. An additional experiment (H_2SO_4-low) was performed without active OH-production from O_3. In the other three coating experiments, SOA was generated via the ozonolysis of α-pinene. The quantities of α-pinene and soot were changed at similar O_3 concentration (306 to 384 ppb) to alter the amount of SOA and soot coating generated. In the SOA-S_{ref} experiment, the initial soot mass (63 ± 6 µg m^{-3}) was comparable to H_2SO_4 experiments (within 80 and 90 µg m^{-3}). In SOA-S_{low} smaller quantities of soot (~13 µg m^{-3}) were injected while α-pinene was kept comparable to SOA-S_{ref} (~60 ppb), and SOA_{high}-S_{high} was performed at about two to three times the soot and precursor concentration as SOA-S_{ref} (soot ~169 µg m^{-3}, α-pinene ~120 ppb). Ten control experiments were performed to evaluate the impact on the soot properties of each compound, process, and protocol used in the coating experiments. These aimed to quantify the effects of soot lifetime and coagulation under dry and humid conditions, of irradiation under dry and humid conditions, and of the presence of O_3 and OH-radicals under humid conditions on particles' physico-chemical and spectral optical properties, with particular emphasis on particle density, size, and light absorption. Further control experiments were performed with non-absorbing submicron ammonium sulphate and sulphuric acid aerosols with well-characterized properties to validate the performance and consistency of the optical and physico-chemical measurements, as presented and discussed by Heuser et al. (2025).

2.1 Protocol of chamber experiments

For the experiments, the chamber was filled with an 80/20-mixture of N_2 (evaporated from liquid N_2; Messer, purity >99.995%) and O_2 (Linde 5.0, purity ≥ 99,999%) at a slight overpressure (ambient conditions +5 hPa) to avoid external contaminations.

Table 1. List of soot ageing experiments. These are separated into the coating experiments, in which coating generation was achieved and studied, and the control experiments. Table columns indicate: the experiment name, the measurement interval after coating formation, the total soot lifetime in the chamber, the initial soot mass concentration, the relative humidity (RH), the ozone (O_3) concentration at the start of the SOA generation, and the SO_2 and α-pinene injected concentrations. The list of digital object identifiers (DOI) for the experimental data are also reported. Those data are available through the Database of Atmospheric Simulation Chamber Studies (DASCS) of the EUROCHAMP Data Centre (https://data.eurochamp.org/data-access/chamber-experiments/) also available via the ACTRIS data portal (https://data.actris.eu/).

Experiment	Measurement interval for aged aerosol (hh:mm)	Total lifetime (hh:mm)	Initial mass concentration [µg m^{-3}]	RH (%)	O_3 [ppb]	SO_2 /α-pinene [ppb]	Dataset DOI
Coating experiments							
H_2SO_4-low	03:03	06:50	90 ± 8	~30	/	273 ± 2	https://doi.org/10.25326/76FN-TA55
H_2SO_4-high1	20:31	24:48	89 ± 9	~30	950 ± 5	260 ± 2	https://doi.org/10.25326/PWHP-ED62
H_2SO_4-high2	20:27	25:16	80 ± 8	~30	955 ± 6	258 ± 2	https://doi.org/10.25326/A18P-JF85
SOA-S_{ref}	20:01	24:43	63 ± 6	~30	384 ± 2	60 ± 16	https://doi.org/10.25326/AK6B-ZA08
SOA_{high}-S_{high}	21:58	27:03	169 ± 18	~30	306 ± 2	120 ± 12	https://doi.org/10.25326/N7S0-S115
SOA-S_{low}	02:03	07:22	13 ± 2	~30	354 ± 2	60 ± 16	https://doi.org/10.25326/BGRM-3554
Control experiments							
Soot coagulation dry 1	21:51	21:51	63 ± 6	/	/	/	https://doi.org/10.25326/8KVR-AA70
Soot coagulation dry 2	25:36	25:36	198 ± 18	/	/	/	https://doi.org/10.25326/M24W-V933
Soot irradiation dry 1	02:05	05:01	67 ± 6	/	/	/	https://doi.org/10.25326/2QRB-4E45
Soot irradiation dry 2	01:03	02:37	58 ± 6	/	/	/	https://doi.org/10.25326/8HT1-WA13
Soot coagulation humid	05:16	07:11	78 ± 8	~30	/	/	https://doi.org/10.25326/WN6E-0272
Soot irradiation humid	04:44	06:46	79 ± 8	~30	/	/	https://doi.org/10.25326/EAQE-VX80
Soot O_3 irradiation humid 1	03:24	07:48	74 ± 7	~30	928 ± 5	/	https://doi.org/10.25326/JRAC-4W36
Soot O_3 irradiation humid 2	02:31	06:03	/	~30	925 ± 5	/	https://doi.org/10.25326/2BD3-Q151
Soot O_3 irradiation humid 3	03:11	07:59	/	~30	992 ± 6	/	https://doi.org/10.25326/9G66-MG61
Soot O_3 irradiation humid 4	02:04	05:31	/	~30	1003 ± 6	/	https://doi.org/10.25326/XJKP-JD08

The combustion aerosol was produced with a miniCAST propane-diffusion flame soot generator (Model 6204 Type C, Jing Ltd., Switzerland), which allows for repeatable soot generations (Heuser et al., 2025; Moore et al., 2014). For all experiments, the propane, mixing N_2, quench N_2, oxidation, and dilution air flows were kept at 0.03, 0, 2, 0.75, and 5 L min^{-1}, respectively, as corresponding to the first operation point of the miniCAST, producing a fuel-lean combustion with a global equivalence ratio of 0.91. Fuel-lean miniCAST soot is widely regarded as representative of diesel and aircraft (kerosene-type) emissions (Ess et al., 2021; Moore et al., 2014; Saffaripour et al., 2017). The bulk elemental-to-total carbon ratio (EC/TC) of the generated cast soot (CS), hereafter referred to as CS1, was measured at 0.79 ± 0.11, indicating a BC-dominated composition (Heuser et al., 2025). The CS1 was injected into CESAM through an activated carbon denuder for a duration between 30 and 390 seconds, depending on the targeted mass concentration.

The water vapour was injected about 2 hours after the soot to reach a relative humidity of ca. 30%, as steam from a modified pressure cooker filled with ultra-pure water (18.2 MΩ, 3.2ppb TOC, Milipak) (Wang et al., 2011). Ozone was injected directly out of an ozone generator (BMT 802N, BMT MESSTECHNIK GMBH), using bottled O_2 (Linde 5.0, purity ≥ 99,999%). About 40 ppb of Butanol-d_9 (1-Butanol D_9, 98%, Euroisotop) was volatilized and injected, prior to the O_3, using a vacuum line and a glass bulb. The Butanol-d_9 was used as a tracer to monitor the OH-exposure. Following O_3, about 75 to 90 minutes later, the precursors for the secondary aerosol and coating formation were introduced in the chamber volume. The SO_2 (Merck, 99.95%) was injected using a calibrated gas-tight syringe and septum inlets. The H_2SO_4 generation itself was then started by initiating the photochemical hydroxyl radical production by turning on the three Xenon-arc lamps. The light of the lamps is introduced via quartz windows equipped with Pyrex® filters (6.5mm), generating a spectrum close to solar radiation at ground level (Wang et al., 2011). Temperature fluctuations due to the radiation were limited with a cooling system (LAUDA Integral-T 10000 W) to about 1 to 2 K, resulting in a temperature range of 294 to 301 K during experiments. The α-pinene (98%, Sigma-Aldrich) was volatilized using a vacuum line, and a known quantity of the SOA precursor was injected with a glass bubble. Dark conditions and minimal temperature fluctuations between 289 and 291 K required no temperature regulations in the SOA experiments. After 3 hours since the start of secondary aerosol formation, the majority of the α-pinene was consumed (<3 ppb remaining), and the H_2SO_4 coating production was stopped by turning off the lamps. In experiments H_2SO_4-high1/2, SOA-S_{ref}, and SOA_{high}- $S_{high,}$ the coated soot was left in suspension under dark conditions with reduced instrumentation and minimal dilution (about 3 L min-1). After 15 hours, the aged soot was again fully characterized.

At the end of each experiment, the CESAM chamber was evacuated to around 3 10^{-4} hPa to avoid carryover contaminations and stays evacuated between subsequent experiments. The chamber was also additionally cleaned manually at the beginning of each campaign and when changing the chemical system. More details on the experimental protocol for the soot and control experiments are provided in Text S1 and Table S1 in the Supplementary information.

2.2 Measurements

A large complementary set of state-of-the-art instrumentation was used to characterize the physico-chemical and spectral optical properties of the soot aerosol, as well as the thermodynamic state of the volume and its gaseous content. The full instrumentation including details for measurement uncertainties calculations are detailed in Tables S2 and S3, and previously described in Heuser et al. (2025). The majority of online measurements were performed continuously throughout experiments with the exception of short disconnections at soot and water vapour injections. During the 15h dark ageing, only the number size distribution was measured continuously. Air sampled out of the chamber during experiments (varying between 3 and 22 L min^{-1}) was compensated with a particle-free N_2/O_2-mixture, leading to a constant dilution of the compounds in the chamber. The main instruments used to characterise the aerosol properties in this work are presented in the following. The aerosol was measured without drying to preserve realistic RH conditions.

The aerosol number size concentration between 19.5 and 881.7 nm over 64 channels ($dN/dlogD_m$; D_m, mobility diameter) was continuously measured at 3-minute resolution with a scanning mobility particle sizer (SMPS, TSI, Kripton^{85} neutraliser, DMA 3080, CPC 3772, with 2.0/0.2 L min-1 sheath/aerosol flow rates). Measurements were corrected for diffusion losses and multiple

charge effects with the instrument software. Total uncertainty on $dN/dlogD_m$ was of the order of 5%. The number size distributions were fitted with log-normal functions to determine the population count (or number) median diameter (CMD).

The aerosol effective density (ρ_{eff}) was derived from measurements with a centrifugal particle mass analyzer (CPMA – Cambustion) and an SMPS (TSI, X-ray neutraliser 3087, DMA 3080, CPC 3775 high). A DMA-CPMA-CPC setup was used to measure the aerosol mass-resolved size distributions as described in Heuser et al. (2025) and Yon et al. (2015). Multiple measurements between 0.03 to 6 femtograms allowed for the calculation of the effective density over the range of soot diameters $\rho_{eff}(D_m)$ (Kasper, 1982; Park et al., 2003). The uncertainty on $\rho_{eff}(D_m)$ was estimated to be 10%. A complete DMA-CPMA-CPC scan to derive a full $\rho_{eff}(D_m)$ curve lasted about 35 minutes. The scans were performed after soot injection in the chamber, after each compound injected in the chamber and for coated soot, before and after long-term ageing. The $\rho_{eff}(D_m)$ data were fitted with a power-law relation (Park et al., 2003)

$$\rho_{eff}(D_m) = a D_m^{D_{fm}-3} \quad (1)$$

to determine the mass-mobility exponent (D_{fm}) and the pre-factor a. The D_{fm} is dependent on the morphology of the aerosols (it equals to 3 for spherical-void free particles, and is around 2.2 for soot (Maricq and Xu, 2004; Sorensen, 2011)) and, together with ρ_{eff}, was used as a proxy for morphological and chemical evolution of the soot over the simulated ageing processes (Park et al., 2003; Sorensen, 2011). The $\rho_{eff}(D_m)$ was used to determine the total aerosol mass concentration (m_{total}) as:

$$m_{total} = \sum_i \frac{\pi}{6} {D_{m,i}}^3 \frac{dN}{dlogD_{m,i}} dlogD_{m,i}\, \rho_{eff}(D_{m,i}) \quad (2)$$

where $\rho_{eff}(D_{m,i})$ indicates the values extrapolated at the D_m values of the SMPS and $dN/dlogD_m$ is the corresponding measured number size distribution (the subscript i in Eq. (2) indicates the SMPS channel). As discussed in Heuser et al. (2025), the m_{total} compared well with gravimetric measurements from a tapered element oscillating microbalance (TEOM 1400a – Thermo Scientific). Noteworthy, the mass concentration calculated with Eq. (2) lacks sensitivity to ongoing aerosol physico-chemical processing due to the coarse time resolution of ρ_{eff} measurements.

Morphological information of the soot particles were also retrieved using transmission electron microscopy (TEM). Soot particles samples were collected over different moments of the experiments using three TEM grids (200-mesh copper grid with a Formvar/ carbon film, Agar Scientific) glued onto the Teflon-pore filters (47mm Nuclepore Whatman, 0.8 μm nominal pore size). Sampling was performed with a custom-made stainless-steel filter holder operated at a flow rate of 2-4 L min^{-1}. The total sampling time was adjusted to ensure similar area loadings between different samples. Nevertheless, the total number of TEM images acquired varied considerably among experiments and particularly for the aged conditions, ranging from a few tens to more than 300 images per sampled grid set. The TEM images were acquired with a JEOL® 100CXII and a JEOL® JEM2010 microscopes and processed using the same protocol as described in Heuser et al. (2025). A qualitative visual assessment of the TEM images was performed to characterize the aged sampled soot. However, the variation in the number of images across experiments precluded a statistically robust clustering analysis and, by consequence, a more quantitative comparison across the various experimental stages.

A single particle soot-photometer (SP2 – Droplet Measurement Technologies, 1–min resolution, (Stephens et al., 2003)) was used to measure the refractory mass concentration (m_{rBC}) and its size distribution between 89 and 567 nm (volume equivalent diameter, D_{ve}), assuming a material density of 1.8 g cm^{-3}. The SP2 was calibrated with fullerene-soot material, mass-selected with the CPMA. The calibration curve of fullerene showed comparable coefficients to the most elemental CS1 particles produced at fuel-lean conditions (Heuser et al., 2025). The measured size distributions from the SP2 were extrapolated based on a lognormal fit to

approximate m_{rBC} over the full soot size range (Liu et al., 2014). The uncertainty on m_{rBC} was estimated to be 17%. The ratio of the m_{total} to the SP2 fullerene-calibrated m_{rBC} ($R=m_{total}/m_{rBC}$) was determined for each experiment prior to coating formation and ranged from 1.2 to 1.8. This ratio was used to convert m_{rBC} into the total soot mass (m_{soot}) representing the total carbonaceous mass of soot, including both elemental and organic carbon fractions, according to $m_{soot}=R\cdot m_{rBC}$. This approach enabled continuous tracking of the soot mass concentration throughout the experiments. Due to instrumental limits of the SP2 scattering detector, a detailed quantification of the coating thickness (leading-edge-only, LEO-fit) or frequency of thinly and thickly coated rBC cores (delay-time) was not possible, as reported for the same SP2 instrument in a recent experiment in the AIDA (Atmospheric Interactions and Dynamics in the Atmosphere) chamber (Zanatta et al., 2025).

Spectral optical properties were monitored with a nephelometer (TSI Model 3563 Integrating Nephelometer, 1–sec resolution, sampling flow rate 2 L min^{-1}, Anderson et al. (1996)), providing the scattering coefficient (b_{scat}) at 450, 550, and 700 nm, and two Cavity Attenuated Phase Shift monitors (CAPS PMex, Aerodyne Research, both operated at 1–sec resolution, sampling flow rate 0.85 L min^{-1}, Kebabian et al. (2007), Massoli et al. (2010)) measuring the extinction coefficient (b_{ext}) at 450 and 630 nm. Two additional CAPS single scattering albedo monitors (CAPS PM_{SSA}, 1–sec resolution, sampling flow rate 0.85 L min^{-1}, Onasch et al. (2015), Yu et al. (2024)) were additionally deployed in some experiments to provide b_{ext} at 450 and 630 nm to compare against CAPS PMex data (the scattering signal from the CAPS PM_{SSA} was not considered in this analysis). The b_{ext} by the CAPS PMex and PM_{SSA} agreed within their uncertainty (<6%). The aerosol scattering coefficient measured at angles between 7° and 170° from the nepheleometer was corrected based on Massoli et al. (2009) to obtain the fully integrated 0-180° b_{scat} by using a real refractive index of 1.95 (Bond and Bergstrom, 2006). Total uncertainty on b_{sca} was estimated at about 8%. The scattering Ångström exponent was calculated via the power-law fit of the spectral b_{scat} and used to interpolate the scattering coefficient at 630 nm.

The aerosol absorption coefficient (b_{abs}) at 450 and 630 nm was calculated from online measurements throughout each experiment as b_{ext} from the CAPS PMex minus b_{scat} from the nephelometer. The uncertainty on the derived b_{abs} was estimated to range within 10-30%. As fully described in Heuser et al. (2025), the b_{abs} derived with extinction-minus-scattering was compared against three filter-based measurements operating between 375 and 850 nm: the Multi Angle Absorption Photometer (MAAP, Petzold et al. (2005)), the Multi-Wavelength Absorbance Analyzer (MWAA, Massabò et al. (2013)), and the polar photometer of the University of Milano (PP_UniMI, Vecchi et al. (2014)). The comparison of the b_{abs} at 450 and 630 nm shows an average difference of 7% and a strong correlation of $R^2=0.94$ between extinction-minus-scattering and filter-based techniques, which is within the combined measurement uncertainty. Greater data dispersion was observed for absorption coefficients below 10 Mm^{-1}, a value that can be considered the lower detection limit for b_{abs}. During the experiments, the measured absorption coefficients ranged from 10 to 10^3 Mm^{-1}, indicating that the entire range of b_{abs} values in the present analysis falls within the reliable measurement range.

The gas phase composition was measured during the experiments using a set of gas monitors measuring the concentrations of SO_2 (Horiba APSA370), O_3 (Horiba APOA370), $NO_X/NO_2/NO$ (Horiba APNA370), NO_2 (Teledyne T500U), and CO/CO_2 (APEE – ProCeas). To follow the content of α-pinene and butanol-D_9 compounds a Proton Transfer Reaction Time of Flight Mass Spectrometer (PTR-ToF-MS, Kore Technology, Jordan et al. (2009)) was used. The atmospheric state of the chamber was tracked throughout the experiments by measurements of the pressure (Baratron type MKS 626AX13TDE (high range)/ 626AX11TDE (low range)), temperature, and relative humidity (Vaisala HMP234- Hygrometer).

2.3 Data analysis

2.3.1 Experimental evaluation of the absorption enhancement (E_{abs}) and coating-to-soot mass ratio ($M_{R,bulk}$)

Online data were averaged over common base time intervals of 3 minutes, a value about double the typical mixing time of the chamber, and all volumetric quantities were converted into standard pressure and temperature conditions (1013.25 mbar, 273.15 K).

The mass absorption cross section (MAC) of the soot particles was calculated at 450 and 630 nm at 3-minute resolution for each experiment as the ratio of the b_{abs} and m_{soot}. The uncertainty on the 3-min MAC was determined as the propagation of the uncertainty of b_{abs} (±10-30%) and m_{soot} (±26%) and averages at about 30%, increasing throughout each experiment with decreasing the number and mass aerosol concentration. The absorption enhancement factor E_{abs} was calculated at 450 and 630 nm and 3–min resolution as the ratio of the MAC after the coating generation to its value prior to coating generation ($E_{abs}= MAC_{coated}/MAC_{prior}$). The MAC_{prior} was estimated for each experiment as the average MAC for the 60-90 minutes prior to the precursor injection and the start of the secondary aerosol generation. The uncertainty of E_{abs}, estimated with error propagation from the MAC values, was estimated on average at about 35%.

The measurements from the SMPS, CPMA and SP2 were combined to retrieve the bulk coating-to-soot mass ratio ($M_{R,bulk}$) at 3–min resolution during experiments. The $M_{R,bulk}$ is the ratio of the secondary aerosol mass deposited on the soot either due to condensation or coagulation ($m_{deposited}$) and the soot mass (m_{soot}) ($M_{R,bulk}=m_{deposited}/m_{soot}$). The $m_{deposited}$ was retrieved by subtracting the m_{soot} (as derived from SP2 measurements) and the mass of secondary aerosol resulting from nucleation (m_{nuc}) from m_{total} as:

$$m_{deposited} = m_{total} - m_{soot} - m_{nuc} \quad (3)$$

The m_{total} was determined from full integration of (Eq. 2), while the m_{nuc} was calculated by integrating Eq. (2) over the size range of nucleating secondary aerosol and using the corresponding effective density from CPMA measurements. For the coated aerosol the first size-resolved $\rho_{eff}(D_m)$ measurement was performed about 60 minutes after coating generation, i.e. for already significantly processed/coated soot, then repeated after 15h ageing. The $M_{R,bulk}$ is therefore the most reliable around these $\rho_{eff}(D_m)$ scans and beyond this point is an approximation that is only sensitive to significant coating evolution via size changes. To minimize bias and potential misinterpretation, the $M_{R,bulk}$ values were only considered after an initial processing period of 15 minutes, when most significant evolution in the coating experiments is expected. The uncertainty on $M_{R,bulk}$ was estimated as the propagation of the uncertainties of the individual masses and averages at around 50%, increasing, as for the MAC, throughout the experiments due to the dilution of the chamber volume.

2.3.2 Mie core-shell calculations of E_{abs} versus $M_{R,bulk}$

The E_{abs} was also theoretically calculated using the Mie-core-shell optical theory for varying $M_{R,bulk}$ to compare one of the most common modelling approaches with our measurements. In the Mie core-shell an aerosol particle is represented as a volume-equivalent sphere coated with a homogeneous layer with a uniform thickness. This enables the representation of the coated particles via an inner diameter (core particle) and a total diameter (particle/core and coating/shell).

The Mie core-shell calculations were done by assuming that the soot particles have a homogeneous size-independent composition. Additionally, a fixed reference soot number size distribution was chosen to represent the aerosol core, translated from mobility size to volume-equivalent size based on the $\rho_{eff}(D_m)$ measurements and the derived material density of the soot (Heuser et al.,

2025). The size distribution taken just prior to SO_2 injection during the H_2SO_4-high1 experiment was chosen as a representative soot core distribution. The outer diameter due to coating formation on soot was determined using the densities of the soot, H_2SO_4, and α-pinene SOA calculated from the measured $\rho_{eff}(D_m)$. Refractive indices for the core and the shell were taken from the literature and from CESAM experiments. For the core soot, two complex refractive index (m=n-ik) values were used at 450 and 630 nm: (i) the most commonly assumed value for BC of 1.95-0.79i (Bond and Bergstrom, 2006) and (ii) a second value of 1.46-0.3i (Habib and Vervisch, 1988) selected to actively represent a value on the other end of the complex refractive index range generally associated with soot. For the H_2SO_4 coating, values of the complex refractive index were retrieved from control experiments described in Heuser et al. (2025), in which a value of 1.30-0i (450 nm) and 1.24-0i (630 nm) was found to best describe the H_2SO_4 generated in CESAM at 30% relative humidity. For the α-pinene SOA, a wavelength-independent real part of 1.5 with a negligible imaginary part was used based on previous studies (Denjean et al., 2015; Kim et al., 2010; Schnaiter et al., 2005).

To determine the E_{abs} at different $M_{R,bulk}$, the b_{abs} was calculated once for an uncoated aerosol using classical Mie theory and the size distribution of the soot core and then with Mie-core-shell for progressively increasing outer diameters for varying $M_{R,bulk}$ from 1 to 5 in 0.1 steps. The $E_{abs}(M_{R,bulk})$ was calculated as the ratio of the b_{abs} of the coated and uncoated soot for the given $M_{R,bulk}$.

3. Results

The time evolution of number size distribution, CMD, $M_{R,bulk}$, and E_{abs} at 630 nm, as well as TEM pictures for the fresh, coated, and aged soot particles for the H_2SO_4 and the α-pinene SOA coating experiments are shown in Fig. 1 and 2. Timelines for all the H_2SO_4 and SOA coating experiments, also including E_{abs} at 450 nm, are shown in Fig. S2-S3, and S11-S16 of the supplementary information. Timelines and results of the ageing control experiments are shown in the supplementary figures S17-S23. The size-resolved $\rho_{eff}(D_m)$ measured for the different control and coating experiments is shown in Fig. 3. Table 2 synthesises the physico-chemical and optical properties of the fresh, coated and aged soot aerosols.

3.1 Pre-coating soot evolution and ageing control experiments

The start point for the experiments is an about two-hour-old soot aerosol for which a complete set of properties was measured to determine an initial reference. In its fresh state the investigated soot has a lacy fractal morphology, as shown in TEM images (Fig. 1e, 2e), quantified by a mass-mobility exponent D_{fm} of 2.11 ± 0.04. The soot shows a mono-modal size distribution with an initial count median diameter CMD around 100-120 nm, increasing to values between 150 and 250 nm due to coagulation within the first 2 hours of experiments (Fig. 1a, 2a). For the CMD of 200 nm the fresh soot particles have an average ρ_{eff} of 232 ± 13 kg m^{-3} (Fig. 3). The soot mass concentration at the end of this characterisation and just prior to the water vapour injection ranges between 13 and 169 µg m^{-3}.

As shown in Fig. 1a and 2a, no significant changes in the CMD or number concentration are observed due to water vapour injection, with the exception of minimal loss of particles that can be attributed to a physical washout and the short pressure change in the chamber. Similarly, no significant effect on the soot physico-chemical is observed due to ozone injection and the following 2-3 hours prior to the H_2SO_4 and SOA generation. Measurements of $\rho_{eff}(D_m)$ show only slight differences, within uncertainties, between pre-coating steps and fresh soot (Fig. 3), indicating no significant chemical or morphological changes. The MAC values show a consistent minor declining trend during the pre-coating steps, as indicated by the decrease of E_{abs} (Fig. 1d, 2d). This decrease

remains however well inside one standard deviation of the MAC values of fresh soot. To account for this minor evolution, as described in Sect. 2.3.1, the reference MAC_{prior} to calculate E_{abs} is taken by averaging values over the last undisturbed suspension period prior to the coating generation, corresponding to about 60 to 90 minutes.

No significant changes in the soot physico-chemical and optical properties are likewise observed for the control experiments for the various conditions tested. The effective density measurements (Fig. 3a) and the mobility exponents determined from them are found to be rather stable compared to the fresh soot and the pre-coating steps. The only exception was a moderate increase in $\rho_{eff}(D_m)$ observed during the irradiated humid experiments, both in absence and in presence of ozone (Fig. S22-23). These changes in effective density indicate that some, albeit minor, physicochemical transformations occurred during the experiments. Specifically, illumination under humid conditions may promote the photooxidation of surface organic carbon, as previously reported by Han et al. (2012). In the humid experiment with ozone, the increase in effective density is likely associated with ozone uptake by the particles, consistent with previous chamber studies (Kamm et al., 1999; Zelenay et al., 2011). The long-term ageing control experiments, named Soot coagulation dry 1 and 2, also showed some deviations for D_{fm}, with values around 1.96±0.01. These deviations are however attributed to measurement bias due to the very low aerosol concentrations after 24 hours of coagulation and dilution. The MAC values remain for all conditions inside one standard deviation of the values of fresh soot as reported in Heuser et al. (2025) (Fig. S1).

3.2 Soot-H_2SO_4 coating and ageing

As shown in Fig. 1a and 1b, the start of the H_2SO_4 generation leads to a progressive increase of soot CMD due to the condensation of coating material on the particles, reflected in a marked increase of the soot ρ_{eff} (Fig. 3b), as well as to the production of new modes associated with homogeneous particle formation below CMDs of 120 nm. The estimated H_2SO_4 mass deposited on the soot due to condensation, but also coagulation with the H_2SO_4 mode, is quantified via the bulk coating-to-soot mass ratio $M_{R,bulk}$ (Fig. 1c). The H_2SO_4-low condition (lower OH oxidant availability) produces lower coating mass with $M_{R,bulk}$ increasing from a value of about 1.0 roughly 15 minutes after the beginning of H_2SO_4 generation, to 1.2 about 3 hours later. Conversely, the H_2SO_4-high conditions (higher OH availability) lead $M_{R,bulk}$ to a quick rise to around 2.0-2.2 and a continuous increase to 3.5-3.9. The continued accumulation of coating material on soot induces a progressive increase in absorption (Fig. 1c-d). The E_{abs} values at 630 nm average at a maximum of around 1.3-1.4 (Fig. 1d), with values at 450 nm exceeding 1.5 (Fig. S2).

The retrieved average D_{fm} ranges from 1.89 to 2.01, and remains comparable with the value for fresh soot, indicating minimal changes to the shape of the lacy fractal particles after the initial coating addition. Nonetheless, TEM images depict a more heterogeneous mixing state, with both partial and fully coated particles, and both compacted and fractal-like soot (Fig. 1f; more illustrative images are shown in Fig. S4).

A decrease in E_{abs} down to about 1.0-1.3 is measured at both wavelengths after 15 hours of simulated dark ageing of the coated soot (grey area Fig. 1b-1d, Fig. S2), despite the $M_{R,bulk}$ showing no significant differences. The decrease in E_{abs} is likely associated to a size reduction of the absorbing soot core, as observed in TEM images analysis (Fig. 1g, Fig. S4), showing significant particles' restructuration. This restructuration is assumed to be caused by the continued accumulation of coating on the soot by condensation and coagulation, which homogenises the soot core structure while the $M_{R,bulk}$ remains relatively unchanged. This continuous coating formation is supported by a slight observed increase of both CMD and ρ_{eff} (Fig. 3b), and a decrease in residual O_3 and soot number concentration.

Table 2. Physico-chemical and optical properties of the fresh and the coated soot aerosol. The given properties of the fresh soot are retrieved in Heuser et al. (2025) and corresponds to soot after 60 min in suspension in the CESAM chamber. The properties of the coated soot aerosols are given at two stages: the *coated*, representing the average of soot properties between 15 and 240 minutes after coating formation, and the *aged*, representing the coated soot properties averaged between 1000 and 1300 min after coating formation, i.e. after the long-term ageing. The average and standard deviation of the bulk coating-to-soot mass ratio ($M_{R,bulk}$) and the absorption enhancement (E_{abs}) at 450 and 630 nm wavelengths are provided. The mobility exponent (D_{fm}) values are reported for the *coated* soot.

Fresh soot aerosol (Heuser et al., 2025)					
		CMD (nm)	**D_{fm}**	**MAC ($m^2\ g^{-1}$)**	
				450 nm	**630 nm**
		145 ± 12	2.11 ± 0.04	6.0 ± 1.0	4.3 ± 0.7
Coated soot aerosol (this work)					
		$M_{R,bulk}$	**D_{fm}**	**E_{abs}**	
				450 nm	**630 nm**
H_2SO_4-low	*Coated*	1.1 ± 0.1	2.01 ± 0.04	1.12 ± 0.15	1.05 ± 0.03
	Aged	/	/	/	/
H_2SO_4-high1	*Coated*	2.9 ± 0.4	1.89 ± 0.06	1.41 ± 0.18	1.26 ± 0.11
	Aged	3.3 ± 0.4	/	1.02 ± 0.11	1.10 ± 0.09
H_2SO_4-high2	*Coated*	2.6 ± 0.4	1.92 ± 0.06	1.37 ± 0.15	1.29 ± 0.13
	Aged	3.5 ± 0.9	/	1.08 ± 0.2	1.23 ± 0.13
SOA-S_{ref}	*Coated*	1.2 ± 0.1	2.24 ± 0.10	1.19 ± 0.05	1.17 ± 0.04
	Aged	0.5 ± 0.1	/	0.83 ± 0.04	0.85 ± 0.14
SOA_{high}-S_{high}	*Coated*	1.3 ± 0.2	2.06 ± 0.08	1.31 ± 0.03	1.30 ± 0.03
	Aged	0.4 ± 0.1	/	1.00 ± 0.03	1.04 ± 0.03
SOA-S_{low}	*Coated*	3.3 ± 0.2	2.61 ± 0.08	1.32 ± 0.15	1.30 ± 0.08
	Aged	/	/	/	/

3.3 Soot-SOA coating and ageing

In contrast with the slower H_2SO_4 experiments, the injection of the α-pinene precursor in the O_3–rich chamber leads to a quasi-instantaneous start of the SOA generation marked by a rapid appearance and growth of a mode below 100 nm mobility diameter associated with new particle formation (Fig. 2a, ρ_{eff} data Fig. 3c). The start of the SOA generation also marks an increase of $M_{R,bulk}$ due to the condensation of coating material on the soot particles (Fig. 2c), supported by a ρ_{eff} increase in the soot containing fraction above 100 nm diameter. The $M_{R,bulk}$ rapidly reaches an average value of around 3.3 for SOA-S_{low} (experiments with the highest precursor-to-soot-ratio), and of 1.2 to 1.3 for the SOA-S_{ref} (initial soot mass comparable to H_2SO_4 experiments) and SOA_{high}-S_{high} experiments (about twice the soot and precursor concentration than SOA-S_{ref}). The D_{fm} rises to 2.06 ± 0.04 (SOA_{high}- S_{high}), 2.24 ± 0.05 (SOA-S_{ref}), and 2.61 ± 0.04 (SOA- S_{low}), indicating that the coating formation induced a transition towards more spherical and compacted particle morphologies. This restructuring is also reflected by the marked and simultaneous decrease in the CMD for SOA-S_{ref} and SOA_{high}-S_{high}. In contrast, the CMD of SOA-S_{low} increases rapidly after coating formation. The TEM images additionally support the coating-induced soot restructuring in all experiments. They show that the majority of soot collapsed to form small and compact aggregates (Fig. 2f-g; more illustrative images in Fig. S5), and, when visible from microscopy, the coating is identified to encapsulate soot particles. The net increase in CMD observed for SOA-S_{low} is then attributed to the larger amount

of condensed coating material for this experiment, which masks the reduction in particle size associated with soot restructuring (Fig. 2b, Fig. S3). After this initial evolution, the soot CMD for SOA-S_{ref} and SOA_{high}- S_{high} stabilizes as a consequence of minimal further SOA deposition (α-pinene precursor consumed) and negligible coagulation (as discussed in Text S2, Fig. S10). In contrast, for SOA-S_{low} the CMD of the soot peak is found to continuously decrease, interpreted as ongoing restructuration.

The E_{abs} measured at 450 and 630 nm rapidly rises following $M_{R,bulk}$ as the SOA coating on soot establishes. Then, until the ageing, it remains rather stable at values between 1.2 and 1.4 for SOA-S_{ref} (Fig. 2d) and SOA_{high}- S_{high}. Higher E_{abs} up to 2 are measured for SOA-S_{low} right after coating starts due to larger $M_{R,bulk}$, decreasing afterwards following the CMD decrease and its underlying restructuration (Fig. S3).

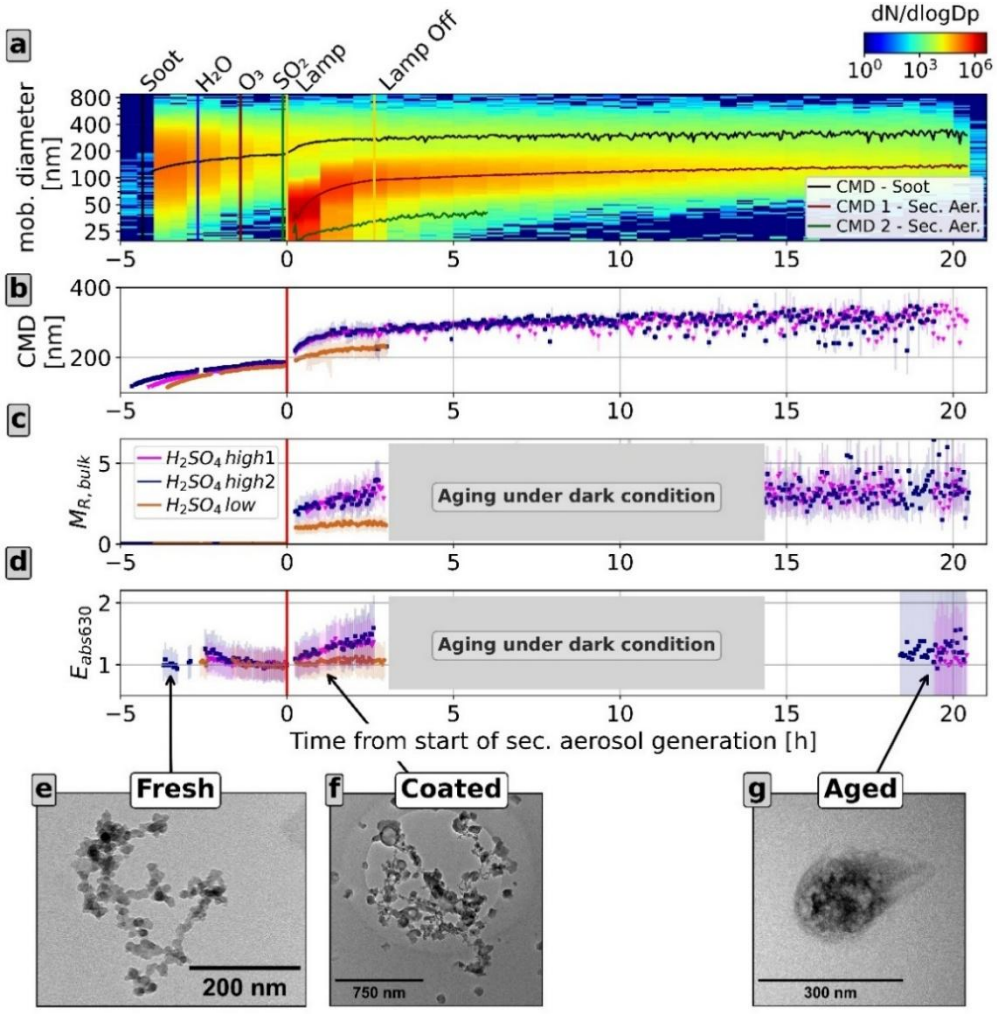


Figure 1. (A): Time evolution of number size distribution as a function of the mobility diameter for the H_2SO_4-high1 experiment (t=0 is the start of the secondary aerosol generation). The evolution of the count median diameters (CMD) of identified modes determined from log-normal fits of the size distribution is overlayed (soot: black, H_2SO_4: red, green). Vertical lines indicate the occurrence of various events during the experiment (injection of soot, water vapour, O_3, SO_2; start and stop of irradiation, indicated as lamp on and lamp off). Time evolution of the (B) count median diameter (CMD) of the soot peak mode, (C) bulk coating-to-soot mass ratio $M_{R,bulk}$, (D) absorption enhancement factor at 630 nm for the H_2SO_4-high1, H_2SO_4-high2 and H_2SO_4-low experiments. (E, F, G): Illustrative TEM pictures for the fresh, coated, and aged soot particles from the H_2SO_4-high1 experiment. Error bars are omitted for clarity.

After 15 hours of ageing in the dark, a significant decrease of $M_{R,bulk,}$ and E_{abs} (0.83-1.04) at rather constant CMD is observed for the SOA-S_{ref} and SOA_{high}- S_{high} experiments. The reduction of $M_{R,bulk}$, concurrently with the absence of further SOA production, negligible coagulation, invariance of CMD, and a slight reduction in the soot density, indicates a loss of coating mass on the particles. Such a loss can occur during the continuous dilution of the chamber volume, despite minimal, which can lead to the evaporation of some of the more volatile compounds of the SOA (Grieshop et al., 2007; Metcalf et al., 2013), while low-volatile organics remain on the soot and continue to affect the absorption (Zhang et al., 2023). Such a loss of coating may cause further compaction of the soot (Corbin et al., 2023), as TEM pictures show dominantly collapsed particles (Fig. 2g). Therefore, the pronounced decrease in E_{abs} (down to values lower than 1) after 15 h of ageing is attributed to the combined effects of coating mass loss through evaporation and continued soot restructuring, which further reduced the particle size relative to the pre-coated soot.

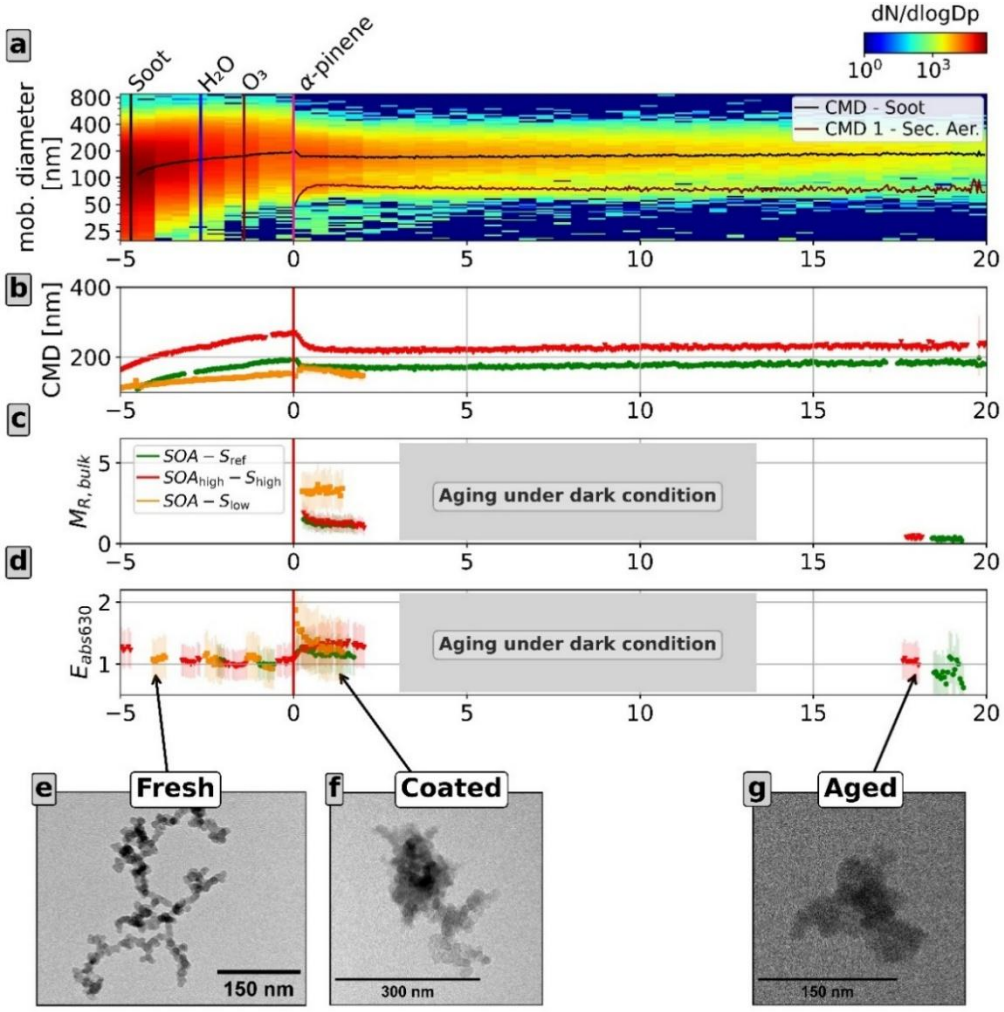


Figure 2. (A): Time evolution of number size distribution as a function of the mobility diameter for the SOA–S_{ref} coating experiment (t=0 is the start of the secondary aerosol generation). The evolution of the count median diameter (CMD) of different identified modes determined from log-normal fits of the size distribution is shown (soot: black, SOA: red). Vertical lines indicate the occurrence of various events during the experiments (injection of soot, water vapour, O_3, and α-pinene). Time evolution of the (B) count median diameter (CMD) of the soot peak mode, (C) bulk coating-to-soot mass ratio $M_{R,bulk}$, (D) absorption enhancement factor at 630 nm for the SOA–S_{ref}, SOA_{high}–S_{high}, and SOA–S_{low} experiments. (E, F, G): Illustrative TEM pictures for the fresh, coated, and aged soot particles from the SOA–S_{ref} experiment. Error bars are omitted for clarity.

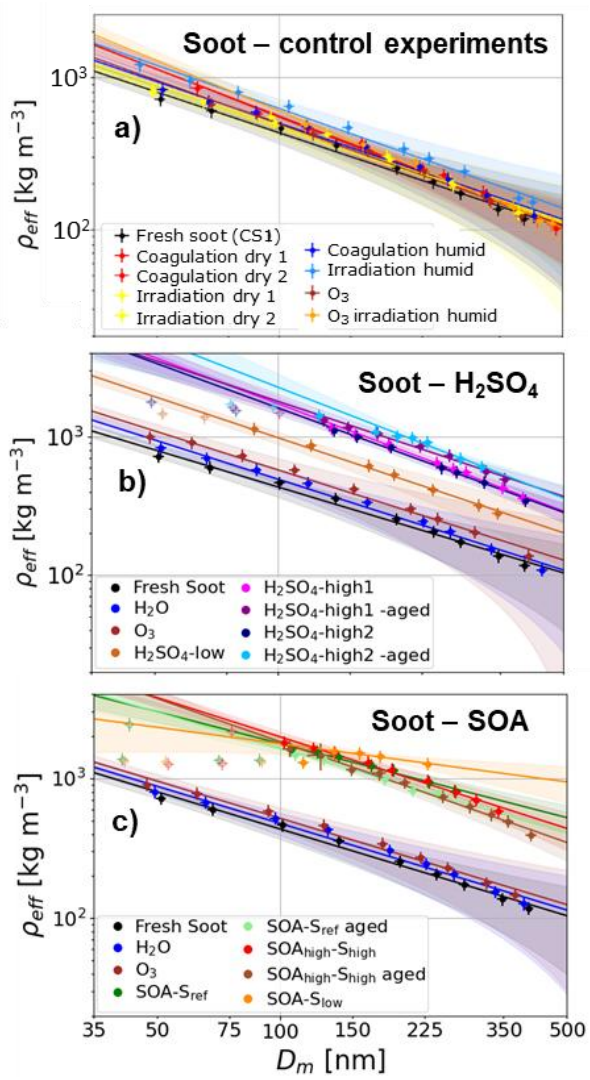


Figure 3. Effective density measured as a function of the mobility diameter, $\rho_{eff}(D_m)$, for (a) the different control experiments, and for (b) the H_2SO_4 and (c) the α-pinene SOA coating experiments. The power-law fits of $\rho_{eff}(D_m)$ based on Eq. 1 (coloured lines) and the fitting uncertainties (coloured-shaded areas) are shown. As a reference, the measurements for fresh soot are shown in (a). Additional plots of $\rho_{eff}(D_m)$ for the coating experiments are provided in Fig. S8. Error bars on single data points are omitted for clarity.

4. Discussion

4.1 Impact of coating dynamics and morphological restructuring on E_{abs}

The results presented in this work evidence that E_{abs} depends not only on the quantity of coating material deposited on the soot, but also on size and morphological modifications that affect E_{abs} magnitude and evolution, modulated by different coating dynamics and ageing.

In the experiments, larger E_{abs} are observed when aggregate shapes are more widespread and lacy aggregates are present. On the contrary, lower E_{abs} for given $M_{R,bulk}$ are measured for all conditions with more compacted soot aggregates. This is especially

prominent when comparing the clusters of the observations of SOA-S_{ref} and SOA_{high}-S_{high} and can be explained by the collapse of the soot aggregate, reducing particle size and optical absorption cross section (Kahnert and Devasthale, 2011) while the coating mass remains constant. Morphological restructuration is observed both directly at the early stages of the SOA coating and for aged H_2SO_4-coated soot, indicating that E_{abs} can evolve further after an initial coating formation. This size effect can be strong enough to reduce the E_{abs} to values lower than the pre-coating state (<1) even with light coatings, as for aged SOA-coated soot.

The shape, i.e. restructuration of the particles, and the coating distribution are found to vary with experiments and ageing time. The slower production of H_2SO_4 impacts the shape and thus the morphology of the soot less in the initial coating formation stages than the much faster SOA formation, which rapidly reduces mobility diameter and compacts soot particles. Only after long term ageing, the majority of particles for H_2SO_4 experiments is restructured, accompanied by a reduced E_{abs} for the aged and collapsed H_2SO_4-coated soot. Based on previous flow reactor-type measurements observing soot compaction during rapid H_2SO_4 condensation (Khalizov et al., 2009b; Zhang et al., 2008), it can be assumed that the difference is not purely compound-related but likely a result of the dynamics of the coating formation.

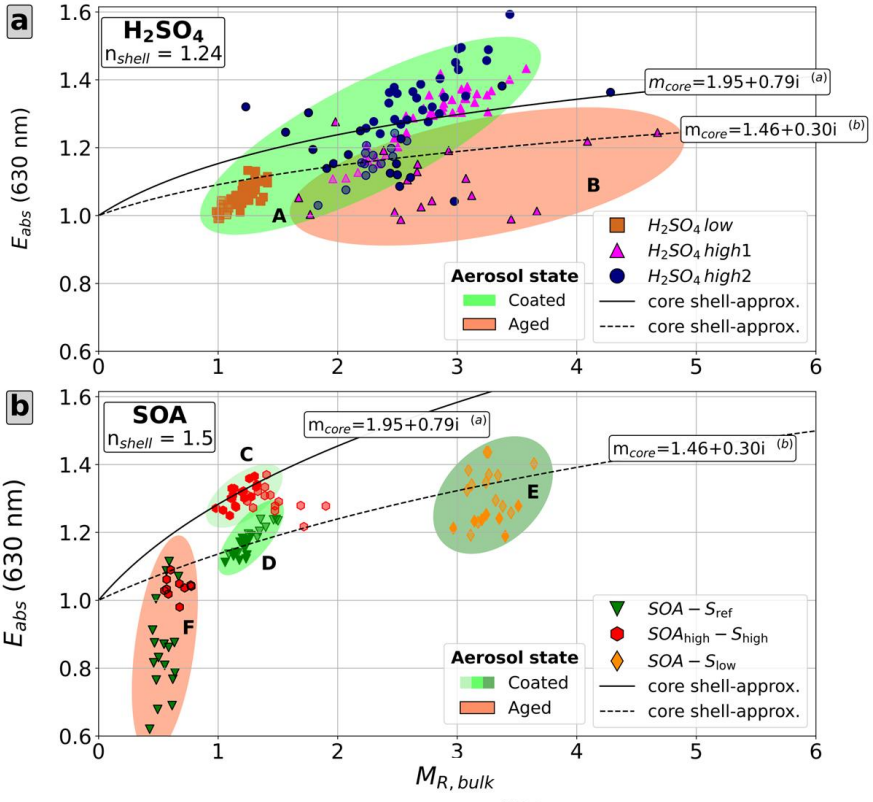


Figure 4. Absorption enhancement factor (E_{abs}) at 630 nm as a function of the coating-soot mass ratio ($M_{R,bulk}$) for (A) the H_2SO_4 and (B) the α-pinene SOA coating experiments. Symbols and color separate the measured data of different experiments. Slightly transparent values are measured during the initial 60 minutes and points with black edges are taken after the ageing. Groupings of pre- (green) and post-ageing (red) values are manually highlighted using coloured ellipses. Additionally, the theoretical calculations using the Mie core-shell approximation for the different coating types are shown. The EF-core-shell curve is shown for the value of the real part corresponding to the refractive index associated to the coating material: a value of n_{shell}=1.5 for the SOA and n_{shell}=1.24 for H_2SO_4. The refractive index of the soot core (n_{core}) is set at a) 1.95 – 0.79i, representative of BC based on Bond and Bergstrom (2006), and at b) 1.46-0.3i (Habib and Vervisch, 1988), representing a value on the other end of the refractive index range associated with soot. Error bars are omitted for clarity. A version of this figure including error bars is shown in Fig. S7.

4.2 Misprediction of the absorption enhancement by core-shell and fixed E_{abs} assumption

Experimental observations in the present study suggest that the E_{abs} can be significantly mispredicted if restructuration and size changes are not taken into account, a process frequently observed in ambient observations (Colbeck et al., 1990; Corbin et al., 2023; Fierce et al., 2020; Khalizov et al., 2009a; Wang et al., 2023). However, this is not possible with the commonly used idealized Mie calculations, as they rely on volumetric-based sizing, nor with fixed E_{abs} approximation. Implications of this drawback are visualized in Fig. 4 (630 nm) and Fig. S6 (450 nm), which each contain two predictions of the E_{abs} - $M_{R,bulk}$ relation based on Mie core-shell calculations for each of the two coating types. The calculated curves differ in the refractive index assumptions for the soot core, which was selected to represent both pure BC and soot, as well as values with contrasting real and imaginary components. The effect of changes in morphology is best shown in the SOA results (Fig. 4b), where clusters of E_{abs} at the same $M_{R,bulk}$ can be observed. These can be described as core-shell by varying the refractive index, even though neither the soot's nor the coating's intrinsic optical properties change between experiments. The cases for which the modelled E_{abs} align more closely with measured ones are conditions with freshly well-established coatings. While for SOA they happen instantly, for H_2SO_4, this only applies for conditions with higher $M_{R,bulk}$ ($2< M_{R,bulk} <3.5$). This is in line with the observations of Liu et al. (2017) showing that a sufficient enhancement is only possible when a certain mixing ratio or threshold is reached. In this case, a core-shell internal mixing approximation may be potentially suitable for describing it. Observations from this study show that, in the range of $M_{R,bulk}$ investigated, the core-shell approximation fails to predict E_{abs} for the other conditions, i.e., uncollapsed partially coated soot with significant particle-to-particle heterogeneity and aged coated particles. Previous works using both models and experimental studies have shown that the distribution of the coating and position of the soot in the coated particles (e.g., partial coating, embedded soot) can have a significant impact on the absorption enhancement and that the shape of the particle can influence this distribution (Adachi et al., 2010; Fierce et al., 2016, 2020; Liu et al., 2017; Zhang et al., 2025). Adachi et al. (2010) noted relevant inhomogeneity in particle-coating mixing, particularly for elongated non-collapsed particles. Such an inhomogeneity is likely the cause of the systematic differences between the observed and core-shell predicted E_{abs}, in particular during a slow coating generation.

Compared to experimental observations, the E_{abs} predictions at 630 nm overestimate absorption by up to 60% in the Mie-based retrieval, and by up to 40% for the, commonly used, fixed E_{abs} value of 1.5, but increasing up to 75% for fresh partial coatings or soot that has undergone restructuration. Experimental conditions characterized by established coating and only limited soot restructuring exhibit improved agreement between predicted and measured E_{abs} values, although underestimations between 2% and 30% persist.

4.3 Comparison to previous chamber studies investigating soot ageing

Only a limited number of chamber studies have examined both the formation and subsequent ageing of coatings on soot particles. Although their soot generation methods, coating protocols, and the extent of soot and coating characterization differ from those employed in the present study, two studies, the ones by Schnaiter et al. (2005) and by Metcalf et al. (2013), investigated the formation and ageing of organic coatings on polydisperse soot and are discussed below. To the best of our knowledge, no comparable chamber studies examining the formation and ageing of sulfuric acid coatings on soot have been reported.

Schnaiter et al. (2005) investigated the impact of α-pinene SOA coatings on diesel soot using experiments conducted in the 84 m³ AIDA chamber. In their study, the soot underwent five successive coating steps through the in situ ozonolysis of α-pinene before being aged for an additional 10 h in the chamber, resulting in total experiment durations of up to 25 h. They reported absorption enhancement factors of 1.8-2.1 at wavelengths of 450, 550, and 700 nm for collapsed soot aggregates. These values are at the upper end of the range observed in our SOA experiments, particularly for the SOA-S_{low} experiment, which most closely resembles the conditions in terms of the soot-to-α-pinene precursor ratio as investigated at the AIDA chamber. In contrast to our observations, Schnaiter et al. (2005) found that E_{abs} remained nearly constant during the ageing period. This discrepancy is likely explained by fundamental differences in the experimental protocols, particularly the ageing conditions. In our experiments, the aerosol was aged under slight continuous dilution and in the absence of additional α-pinene precursor. Under these conditions, the more volatile SOA components gradually evaporated, leading to a reduction in the coating mass. In the AIDA experiments, however, the soot experienced continuous SOA growth throughout the ageing period. This was achieved by first introducing ozone into the chamber and subsequently supplying a continuous flow of air saturated with α-pinene vapor, thereby sustaining ongoing SOA condensation onto the soot particles. These conditions maintained the particle coating and likely explain why E_{abs} remained nearly constant during the 10 h ageing period. Schnaiter et al. (2005) further showed that the Mie core–shell model cannot accurately reproduce the optical behaviour of thinly coated soot particles, although its agreement with observations improves with increasing coating-to-soot ratios.

Metcalf et al. (2013) performed chamber experiments with fullerene soot, a surrogate for fractal carbonaceous particles, in the 28 m³ Caltech Teflon chamber. The soot was exposed to several types of organic coatings, including SOA formed from the high-NOx photooxidation of naphthalene and from the high- and low-NOx photooxidation of α-pinene. The experiments consisted of an initial irradiation period lasting several hours, during which SOA formed and the chamber temperature increased, followed by several hours of dilution accompanied by a gradual decrease in temperature. Consistent with our observations, Metcalf et al. (2013) reported absorption enhancement factors of 1.25–1.35 at 405 nm and 1.15–1.30 at 781 nm for the α-pinene SOA experiments. They also observed that the SOA coating partially evaporated during the course of the experiments, particularly during the dilution phase. The extent of evaporation depended on the chamber temperature, both during the irradiation period, which influenced the formation of more or less semi-volatile SOA components, and during dilution, where the magnitude of the temperature decrease controlled the degree of evaporation. In our experiments, temperature variations during dilution were limited to 1–2 K, suggesting that changes in coating mass were primarily driven by dilution rather than by temperature-induced volatility changes. Unlike our observations, Metcalf et al. (2013) demonstrated that E_{abs} can be accurately predicted when the coating mass or thickness is known and the particle can be represented by a simple core–shell geometry. However, this approach relies on fullerene spherical particles instead of fractal soot, thereby limiting the representativeness of the results for atmospheric conditions.

Overall, these previous studies have provided evidence that coating-induced absorption enhancement occurs and provide key complementary observations to our study. However, they have important limitations because they provide only limited information on the simultaneous evolution of particle coating and morphology throughout the different stages of the coating process and, in the case of Metcalf et al. (2013), rely on simplified particle morphologies. Consequently, it remains difficult to directly compare these studies or derive predictive relationships applicable to atmospheric soot. The present work addresses this gap by systematically characterizing both coating evolution and soot restructuring throughout the ageing process, so to move towards a mechanistic understanding of E_{abs}. Although such measurements are experimentally challenging, this approach provides new insights into the

underlying processes and demonstrates that this combined characterization is essential for developing a predictive understanding of coating-induced absorption enhancement.

5 Implications on radiative forcing estimations

The inability of the Mie core-shell and fixed 1.5 value to systematically predict E_{abs} has consequences for the estimates of the single scattering albedo (SSA, ratio of scattering to extinction) and radiative forcing (RF) for BC-containing aerosols. An illustrative example is given in Table 3 reporting the differences in estimated and measured SSA and the resulting relative differences in RF at 630 nm, for two assumed surface albedos. The SSA in Table 3 was estimated from Mie core-shell theory (SSA_{MieCS}) assuming the same complex refractive indices and particle representation as described in Sect. 2.3.2, or by assuming a fixed E_{abs} of 1.5 ($SSA_{fixed\text{-}1.5}$). To note that in the case of fixed E_{abs}, only the impact of the coating on absorption is considered for the calculation of $SSA_{fixed\text{-}1.5}$, while scattering is assumed unchanged. These values were compared to the measured SSA during experiments (SSA_{meas}). The signal by the SOA and H_2SO_4 nucleating modes was subtracted from the total scattering and extinction when calculating SSA_{meas}. Further details on the SSA calculations are provided in Text S3.

The calculated and measured SSA values were then used to determine the change in RF by utilizing the following equation (Haywood and Shine, 1995), providing the instantaneous forcing for a thin layer of absorbing aerosols at the top-of-atmosphere:

$$RF = -DS_0{T_{at}}^2(1-A_c)\,SSA\beta\delta\left\{(1-R_s)^2-\left(\frac{2R_s}{\beta}\right)\left[\left(\frac{1}{SSA}\right)-1\right]\right\} \quad (4)$$

where D is the fractional day length, S_0 the solar constant, T_{at} the atmospheric transmission, A_c the fractional cloud amount, SSA the aerosol single scattering albedo, β the aerosol upscatter fraction of scattering, δ the aerosol optical depth, and R_s the surface reflectivity. Despite Eq. (4) provides a simplistic estimate of RF considering only aerosol-radiation interactions and not accounting for changes compared to pre-industrial conditions, it can be used to quantify the impact of E_{abs} mispredictions on BC radiative effect. The relative change of RF due to a change from SSA_{meas} and SSA_{MieCS} (or $SSA_{fixed\text{-}1.5}$) was determined as:

$$\Delta RF = \frac{RF_{SSA_{MieCS}}}{RF_{SSA_{meas}}} = \frac{SSA_{MieCS}\left\{(1-R_s)^2-\left(\frac{2R_s}{\beta}\right)\left[\left(\frac{1}{SSA_{MieCS}}\right)-1\right]\right\}}{SSA_{meas}\left\{(1-R_s)^2-\left(\frac{2R_s}{\beta}\right)\left[\left(\frac{1}{SSA_{meas}}\right)-1\right]\right\}} \quad (5)$$

For Eq. (5) two values of R_S (0.2, bare soil, and 0.7, snow/ice) were used as exemplary values. The upscatter fraction β was calculated from a backscattering ratio of 0.27, determined from experimental data using the equations in Moosmüller and Ogren (2017). Calculations for SSA and RF were performed by separating data for fresh coatings (up to 1 hour from the onset of secondary aerosol formation), established coatings (second and third hour), and aged coatings (more than 15 hours). The uncertainty on ΔRF was estimated at ~20% based on the error propagation formula and considering only the uncertainty on the measured SSA (12-25%, Heuser et al. (2025)) and the sensitivity of the modelled SSA on the assumed complex refractive (15% on average based on the comparison of the SSA values calculated with 1.95-0.79i and 1.46-0.3i).

The results in Table 3 show that for conditions that are associated with collapsed soot (H_2SO_4-aged and SOA), the core-shell calculations underestimate the SSA on average between 12 and 56% for early, medium, and latter stages of processing. This underestimation results in an overestimation of the RF averaging at around 46%, but reaching up to 84%, for a bare soil scenario (R_S = 0.2), when compared to RF estimates based on SSA_{meas}. For processing stages where coatings are forming and/or the soot

undergoes limited restructuration SSA values are generally found to be overestimated by 2 to 122%. This indicates that not only is the E_{abs} overestimated by the Mie-based calculations for these conditions, but so is the scattering. These SSA overpredictions lead to an average underestimation of RF of about 17% for the different stages of the experiments in a bare soil scenario. The impact of the SSA misprediction on the RF reduces with increasing surface albedo, being about 20% (collapsed soot) and 10% (inhomogeneous coating and non-collapsed soot) for a surface albedo of 0.7 associated with fresh snow.

The common alternative of a fixed E_{abs} of 1.5 leads to similar SSA and RF mispredictions. Compared to the observations, the SSA at 630 nm is consistently underestimated, in turn leading to an RF overestimation ranging between 6 and 58% in the bare soil and between 4 and 20% for the snow scenario.

Table 3. Average values of the single scattering albedo measured (SSA_{meas}) and calculated at 630 nm based on the Mie core-shell approach (SSA_{MieCS}) for two refractive indices of the soot core (n_{core}) set at 1.95 – 0.79i (Bond and Bergstrom, 2006), and 1.46-0.3i (Habib and Vervisch, 1988) and for fixed E_{abs} of 1.5 ($SSA_{fixed\text{-}1.5}$). The corresponding associated fractional change in radiative forcing, ΔRF, at 630 nm due to the SSA change is reported for varying aerosol processing states of the performed experiments. Data corresponds to a surface albedo (R_S) of 0.2 and 0.7.

Experiment	Time after coating generation [min]	SSA_{meas} measured	SSA_{MieCS} calculated MieCS (1.95-0.79i)	SSA_{MieCS} calculated MieCS (1.46-0.3i)	$SSA_{fixed\text{-}1.5}$ calculated E_{abs}=1.5	ΔRF					
						MieCS (1.95-0.79i)		MieCS (1.46-0.3i)		E_{abs}=1.5	
						R_s 0.2	R_s 0.7	R_s 0.2	R_s 0.7	R_s 0.2	R_s 0.7
H_2SO_4-high1	15 to 60 (coated)	0.18	0.29	0.30	0.13	0.79	0.87	0.75	0.85	1.11	1.07
	60 to 240 (coated)	0.28	0.31	0.36	0.21	0.93	0.96	0.79	0.88	1.20	1.11
	>1000 (aged)	0.35	0.31	0.36	0.27	1.14	1.07	0.97	0.98	1.27	1.13
H_2SO_4-high2	15 to 60 (coated)	0.17	0.29	0.31	0.12	0.77	0.86	0.72	0.83	1.10	1.06
	60 to 240 (coated)	0.30	0.30	0.35	0.22	0.98	0.99	0.86	0.92	1.21	1.11
	>1000 (aged)	0.38	0.29	0.32	0.29	1.34	1.16	1.25	1.12	1.32	1.15
H_2SO_4-low	15 to 60 (coated)	0.11	0.24	0.20	0.08	0.76	0.85	0.83	0.89	1.06	1.04
	60 to 240 (coated)	0.16	0.25	0.22	0.11	0.82	0.89	0.88	0.93	1.09	1.06
SOA-S_{ref}	15 to 60 (coated)	0.37	0.26	0.22	0.28	1.37	1.17	1.50	1.24	1.31	1.14
	60 to 240 (coated)	0.39	0.26	0.21	0.30	1.47	1.22	1.63	1.29	1.33	1.15
	>1000 (aged)	0.35	0.23	0.16	0.27	1.40	1.20	1.62	1.30	1.28	1.14
SOA_{high}-S_{high}	15 to 60 (coated)	0.33	0.27	0.24	0.25	1.19	1.09	1.29	1.14	1.25	1.13
	60 to 240 (coated)	0.37	0.26	0.21	0.28	1.39	1.18	1.54	1.26	1.31	1.15
	>1000 (aged)	0.35	0.22	0.15	0.26	1.40	1.20	1.63	1.31	1.28	1.14
SOA-S_{low}	15 to 60 (coated)	0.49	0.34	0.39	0.39	1.84	1.29	1.58	1.20	1.58	1.20
	60 to 240 (coated)	0.48	0.34	0.39	0.38	1.74	1.27	1.50	1.18	1.55	1.20

6 Summary and concluding remarks

This study provides a laboratory-based investigation to advance the mechanistic understanding of soot E_{abs} and its variability. Taking advantage of the long aerosol lifetime in the CESAM chamber, experiments were designed to explore the relationship between E_{abs} and $M_{R,bulk}$ across a variety of atmospherically relevant processes. The range of E_{abs} observed in this study for polydispersed soot under varying coating and ageing conditions lies within laboratory observations for uniform coating on monodispersed soot (Fierce et al., 2020; Peng et al., 2016) and ambient measurements in background, suburban, and urban environments (Cappa et al., 2019; Liu et al., 2017; Zeng et al., 2024). The $M_{R,bulk}$ extends up to values of 5, representing most common urban and suburban conditions (Cappa et al., 2019; Liu et al., 2017; Zeng et al., 2024), even if values as high as 10 or more are observed in urban and suburban atmospheres and during biomass burning events (McMeeking et al., 2014; Taylor et al., 2020; Wu et al., 2020; Zeng et al., 2024).

Results from the present analysis support the evidence of a correlation between E_{abs} and the coating amount on soot. We highlight, however, the ambiguity of this relation based on experimental observations with varying coating and soot properties. The measured E_{abs} and the corresponding particle physico-chemical properties confirm the impact of the morphological organization of both the soot and the coating-soot system on the E_{abs}. Our controlled laboratory experiments show that the coating formation dynamics, coating type (non-volatile/volatile), and subsequent ageing affect the composition, morphology, and size of the soot and the coating-soot system, whose combined effect ultimately rules the E_{abs} magnitude and its temporal evolution. Based on this dependence, the range of measured E_{abs} cannot systematically be predicted by the Mie core-shell approximation or by a fixed E_{abs} value, as commonly used in models.

Improving radiative forcing predictions requires models to account for the evolution of both particle and coating properties beyond coating thickness alone, in order to capture changes in optical properties, particularly the magnitude of E_{abs} and its evolution. Additional considerations include inhomogeneities in particle coatings, which we found to depend on the coating generation process, as well as the effects of morphological organization of both soot and coatings, which influence the entire soot lifetime.

In order to achieve this objective, previous studies have proposed empirical adjustments of the core-shell model to reconcile with laboratory and ambient observations. These took into account morphological effects to describe single particle mixing state (Fierce et al., 2020; Liu et al., 2017) and particle-to-particle heterogeneity in mixing state (Fierce et al., 2020; Wang et al., 2023; Zeng et al., 2024). While these empirically determined adjustments allow for an improved prediction of the E_{abs}, they are often constrained to specific cases and are limited in general applicability.

More reliable approaches can be envisaged by using more advanced spectral optical theories, such as discrete dipole approximation (DDA), T-matrix, Rayleigh–Debye–Gans for coated fractal aggregate (RDG-CFA), or others (Adachi et al., 2010; Lefevre et al., 2019; Liu et al., 2016; Zhang et al., 2017). As these require detailed information on the soot and coating properties and generally also higher computational resources, they have not found wide use in large-scale models in the past decades. However, recent studies show that progressively increasing consideration of BC mixing state and nonsphericity in models leads to more accurate estimates of BC radiative forcing (Chen et al., 2024; Fierce et al., 2025; Romshoo et al., 2024; Wang et al., 2023; Zeng et al., 2024). In line with these studies, this systematic laboratory investigation stresses the need for more sophisticated approaches than core-shell Mie or fixed E_{abs} approximation to provide accurate calculations of BC absorption enhancement. The physical, chemical, and optical datasets in this study, which are made openly available to the scientific community (all data doi are listed in Table 1),

can provide support for such model developments. The experimental data (such as size, $M_{R,bulk}$, E_{abs}) can be used to test and evaluate model parameterizations, in particular optical modules, and including machine learning and neural network approaches (e.g., Beeler et al., 2026). Nonetheless, more experimental investigation is required, extending to varying chemical systems and ageing conditions. With laboratory experiments being most commonly used for such mechanistic studies, we advise that setups which simulate BC coating formation under very rapid dynamics (such as flow tubes or simulation chambers considering short ageing times) should be used with care, as these approaches may produce overly idealised observations.

Open Research / Data availability

The CESAM data used in this study are available through the Database of Atmospheric Simulation Chamber Studies (DASCS) of the EUROCHAMP Data Centre (https://data.eurochamp.org/data-access/chamber-experiments/, last access: 17 July 2026) also available via the ACTRIS data portal (https://data.actris.eu/, last access: 17 July 2026) with the identifiers listed in Table 1. The core-shell optical calculations were performed with PyMieScatt, which is available at https://github.com/bsumlin/PyMieScatt (last access: 17 July 2026).

Competing interests

The authors declare that they have no competing interests.

Author contributions

CDB and JFD conceived the study. JH, CDB, and JFD designed the experiments and discussed the results. JH conducted the experiments with contributions by CDB, JY, MC, AB, EP, MZ, LR, AM, CY, SC, PL, MM, PF, BPV, and JFD. MM and DF performed transmission microscopy measurements. JH performed the full data analysis under the supervision of CDB and JFD and with contributions from JY, MZ, LR, AM, CY, MC, and DF. BPV, as PI of the CESAM facility, contributed to full experiment realization and management. PL provided the SP2 used in the experiments. JY provided the CPMA used in the experiments. CDB provided funding acquisition and project administration. JH, CDB, and JFD wrote the manuscript. All authors reviewed and commented on the paper.

Acknowledgements

The authors gratefully acknowledge CNRS-INSU, Université Paris Est Créteil, Université Paris Cité, and OSU-EFLUVE for supporting CESAM platform as a component of ACTRIS Research Infrastructure. This platform also benefits from the support of ACTRIS-FR, registered on the Roadmap of the French Ministry of Research. The authors thank AERIS for curating and distributing the data produced by CESAM chamber through ACTRIS portal (https://dc.actris.nilu.no/, last access: 17 July 2026) and ACTRIS DC ASC Unit (formerly known as EUROCHAMP DC, https://data.eurochamp.org, last access: 17 July 2026). Patrick

Ginot is acknowledged for logistic support with SP2 operations. Contributions by Patrick Ausset, Mouad Essani, Gael Noyalet, Vera Bernardoni, Dario Massabò, Federico Mazzei, Brice Temime-Roussel, Roberta Vecchi, and Virginia Vernocchi to experimental activities are gratefully acknowledged. Helpful comments by two anonymous reviewers and by Dr. Schnaiter are gratefully acknowledged.

Funding

This study has been supported by the French National Research Agency (ANR) through the B2C project (contract ANR-19-CE01-0024-01), by the French National program LEFE-CHAT (Les Enveloppes Fluides et l'Environnement – Chimie Atmosphérique) through the BACON project. This work has received funding from the TNA activity of the European Union's Horizon 2020 research and innovation programme through the EUROCHAMP-2020 Infrastructure Activity under grant agreement No 730997. It has also been supported by DIM Qi² and Paris Ile-de-France Region. L. Renzi and M. Zanatta were partially supported by ITINERIS project (IR0000032), the Italian Integrated Environmental Research Infrastructures System (D.D. n. 130/2022 - CUP B53C22002150006), funded by EU - Next Generation EU PNRR- Mission 4 "Education and Research".

References

Adachi, K., Chung, S. H., and Buseck, P. R.: Shapes of soot aerosol particles and implications for their effects on climate, J. Geophys. Res., 115, 2009JD012868, https://doi.org/10.1029/2009JD012868, 2010.

Anderson, T. L., Covert, D. S., Marshall, S. F., Laucks, M. L., Charlson, R. J., Waggoner, A. P., Ogren, J. A., Caldow, R., Holm, R. L., Quant, F. R., Sem, G. J., Wiedensohler, A., Ahlquist, N. A., and Bates, T. S.: Performance Characteristics of a High-Sensitivity, Three-Wavelength, Total Scatter/Backscatter Nephelometer, Journal of Atmospheric and Oceanic Technology, 13, 967–986, https://doi.org/10.1175/1520-0426(1996)013%3C0967:PCOAHS%3E2.0.CO;2, 1996.

Asmi, E., Sipkens, T. A., Saturno, J., Backman, J., Vasilatou, K., Weingartner, E., Keller, A., Ciupek, K., Müller, T., Babu Suja, A., Močnik, G., Drinovec, L., Eleftheriadis, K., Gini, M. I., Nowak, A., and Corbin, J. C.: Mass absorption cross-section of ambient black carbon aerosols - a review, npj Clim Atmos Sci, 9, 17, https://doi.org/10.1038/s41612-025-01288-2, 2025.

Baldo, C., Formenti, P., Nowak, S., Chevaillier, S., Cazaunau, M., Pangui, E., Di Biagio, C., Doussin, J.-F., Ignatyev, K., Dagsson-Waldhauserova, P., Arnalds, O., MacKenzie, A. R., and Shi, Z.: Distinct chemical and mineralogical composition of Icelandic dust compared to northern African and Asian dust, Atmospheric Chemistry and Physics, 20, 13521–13539, https://doi.org/https://doi.org/10.5194/acp-20-13521-2020, 2020.

Baldo, C., Formenti, P., Di Biagio, C., Lu, G., Song, C., Cazaunau, M., Pangui, E., Doussin, J.-F., Dagsson-Waldhauserova, P., Arnalds, O., Beddows, D., MacKenzie, A. R., and Shi, Z.: Complex refractive index and single scattering albedo of Icelandic dust in the shortwave spectrum, EGUsphere, 2023, 1–42, https://doi.org/10.5194/egusphere-2023-276, 2023.

Battaglia, F., Formenti, P., Giorio, C., Cazaunau, M., Pangui, E., Bergé, A., Gratien, A., Pereira, D. L., Bertin, T., de Brito, J. F., Romanias, M. N., Michoud, V., Baldo, C., Chevaillier, S., Noyalet, G., Decorse, P., Picquet-Varrault, B., and Doussin, J.-F.: Formation and composition of organic aerosols from the uptake of glyoxal on natural mineral dust

aerosols: a laboratory study, Atmospheric Chemistry and Physics, 25, 12409–12431, https://doi.org/10.5194/acp-25-12409-2025, 2025.

Beeler, P., Donald, S., and Fierce, L.: DDA-BNN v1.0: A Morphology-Aware Surrogate Model for the Optical Properties of Black Carbon–Containing Particles, EGUsphere, 1–27, https://doi.org/10.5194/egusphere-2026-1270, 2026.

Bond, T. C. and Bergstrom, R. W.: Light Absorption by Carbonaceous Particles: An Investigative Review, Aerosol Science and Technology, 40, 27–67, https://doi.org/10.1080/02786820500421521, 2006.

Bond, T. C., Doherty, S. J., Fahey, D. W., Forster, P. M., Berntsen, T., DeAngelo, B. J., Flanner, M. G., Ghan, S., Kärcher, B., Koch, D., Kinne, S., Kondo, Y., Quinn, P. K., Sarofim, M. C., Schultz, M. G., Schulz, M., Venkataraman, C., Zhang, H., Zhang, S., Bellouin, N., Guttikunda, S. K., Hopke, P. K., Jacobson, M. Z., Kaiser, J. W., Klimont, Z., Lohmann, U., Schwarz, J. P., Shindell, D., Storelvmo, T., Warren, S. G., and Zender, C. S.: Bounding the role of black carbon in the climate system: A scientific assessment: BLACK CARBON IN THE CLIMATE SYSTEM, J. Geophys. Res. Atmos., 118, 5380–5552, https://doi.org/10.1002/jgrd.50171, 2013.

Caponi, L., Formenti, P., Massabó, D., Di Biagio, C., Cazaunau, M., Pangui, E., Chevaillier, S., Landrot, G., Andreae, M. O., Kandler, K., Piketh, S., Saeed, T., Seibert, D., Williams, E., Balkanski, Y., Prati, P., and Doussin, J.-F.: Spectral- and size-resolved mass absorption efficiency of mineral dust aerosols in the shortwave spectrum: a simulation chamber study, Atmospheric Chemistry and Physics, 17, 7175–7191, https://doi.org/https://doi.org/10.5194/acp-17-7175-2017, 2017.

Cappa, C. D., Onasch, T. B., Massoli, P., Worsnop, D. R., Bates, T. S., Cross, E. S., Davidovits, P., Hakala, J., Hayden, K. L., Jobson, B. T., Kolesar, K. R., Lack, D. A., Lerner, B. M., Li, S.-M., Mellon, D., Nuaaman, I., Olfert, J. S., Petäjä, T., Quinn, P. K., Song, C., Subramanian, R., Williams, E. J., and Zaveri, R. A.: Radiative Absorption Enhancements Due to the Mixing State of Atmospheric Black Carbon, Science, 337, 1078–1081, https://doi.org/10.1126/science.1223447, 2012.

Cappa, C. D., Zhang, X., Russell, L. M., Collier, S., Lee, A. K. Y., Chen, C., Betha, R., Chen, S., Liu, J., Price, D. J., Sanchez, K. J., McMeeking, G. R., Williams, L. R., Onasch, T. B., Worsnop, D. R., Abbatt, J., and Zhang, Q.: Light Absorption by Ambient Black and Brown Carbon and its Dependence on Black Carbon Coating State for Two California, USA, Cities in Winter and Summer, JGR Atmospheres, 124, 1550–1577, https://doi.org/10.1029/2018JD029501, 2019.

Chan, T. W., Huang, L., Leaitch, W. R., Sharma, S., Brook, J. R., Slowik, J. G., Abbatt, J. P. D., Brickell, P. C., Liggio, J., Li, S.-M., and Moosmüller, H.: Observations of OM/OC and specific attenuation coefficients (SAC) in ambient fine PM at a rural site in central Ontario, Canada, Atmos. Chem. Phys., 10, 2393–2411, https://doi.org/10.5194/acp-10-2393-2010, 2010.

Chen, G., Liu, C., Wang, J., Yin, Y., and Wang, Y.: Accounting for Black Carbon Mixing State, Nonsphericity, and Heterogeneity Effects in Its Optical Property Parameterization in a Climate Model, JGR Atmospheres, 129, https://doi.org/10.1029/2024jd041135, 2024.

Cheng, Z., Atwi ,K., Onyima ,T., and Saleh, R.: Investigating the dependence of light-absorption properties of combustion carbonaceous aerosols on combustion conditions, Aerosol Science and Technology, 53, 419–434, https://doi.org/10.1080/02786826.2019.1566593, 2019.

Colbeck, I., Appleby, L., Hardman, E. J., and Harrison, R. M.: The optical properties and morphology of cloud-processed carbonaceous smoke, Journal of Aerosol Science, 21, 527–538, https://doi.org/10.1016/0021-8502(90)90129-L, 1990.

Corbin, J. C., Modini, R. L., and Gysel-Beer, M.: Mechanisms of soot-aggregate restructuring and compaction, Aerosol Science and Technology, 57, 89–111, https://doi.org/10.1080/02786826.2022.2137385, 2023.

De Haan, D. O., Hawkins, L. N., Wickremasinghe, P. D., Andretta, A. D., Dignum, J. R., De Haan, A. C., Welsh, H. G., Pennington, E. A., Cui, T., Surratt, J. D., Cazaunau, M., Pangui, E., and Doussin, J.-F.: Brown Carbon from Photo-Oxidation of Glyoxal and SO2 in Aqueous Aerosol, ACS Earth Space Chem., 7, 1131–1140, https://doi.org/10.1021/acsearthspacechem.3c00035, 2023.

Denjean, C., Formenti, P., Picquet-Varrault, B., Pangui, E., Zapf, P., Katrib, Y., Giorio, C., Tapparo, A., Monod, A., Temime-Roussel, B., Decorse, P., Mangeney, C., and Doussin, J. F.: Relating hygroscopicity and optical properties to chemical composition and structure of secondary organic aerosol particles generated from the ozonolysis of α-pinene, Atmospheric Chemistry and Physics, 15, 3339–3358, https://doi.org/10.5194/acp-15-3339-2015, 2015.

Di Biagio, C., Formenti, P., Balkanski, Y., Caponi, L., Cazaunau, M., Pangui, E., Journet, E., Nowak, S., Caquineau, S., Andreae, M. O., Kandler, K., Saeed, T., Piketh, S., Seibert, D., Williams, E., and Doussin, J.-F.: Global scale variability of the mineral dust long-wave refractive index: a new dataset of in situ measurements for climate modeling and remote sensing, Atmospheric Chemistry and Physics, 17, 1901–1929, https://doi.org/https://doi.org/10.5194/acp-17-1901-2017, 2017.

Di Biagio, C., Formenti, P., Balkanski, Y., Caponi, L., Cazaunau, M., Pangui, E., Journet, E., Nowak, S., Andreae, M. O., Kandler, K., Saeed, T., Piketh, S., Seibert, D., Williams, E., and Doussin, J.-F.: Complex refractive indices and single-scattering albedo of global dust aerosols in the shortwave spectrum and relationship to size and iron content, Atmospheric Chemistry and Physics, 19, 15503–15531, https://doi.org/https://doi.org/10.5194/acp-19-15503-2019, 2019.

Di Biagio, C., Doussin, J.-F., Cazaunau, M., Pangui, E., Cuesta, J., Sellitto, P., Ródenas, M., and Formenti, P.: Infrared optical signature reveals the source–dependency and along–transport evolution of dust mineralogy as shown by laboratory study, Scientific Reports, 13, 13252, https://doi.org/10.1038/s41598-023-39336-7, 2023.

Doussin, J.-F., Fuchs, H., Kiendler-Scharr, A., Seakins, P., and Wenger, J. (Eds.): A Practical Guide to Atmospheric Simulation Chambers, Springer International Publishing, Cham, https://doi.org/10.1007/978-3-031-22277-1, 2023.

Ess, M. N., Bertò, M., Irwin, M., Modini, R. L., Gysel-Beer, M., and Vasilatou, K.: Optical and morphological properties of soot particles generated by the miniCAST 5201 BC generator, Aerosol Science and Technology, 55, 828–847, https://doi.org/10.1080/02786826.2021.1901847, 2021.

Fierce, L., Bond, T. C., Bauer, S. E., Mena, F., and Riemer, N.: Black carbon absorption at the global scale is affected by particle-scale diversity in composition, Nat Commun, 7, 12361, https://doi.org/10.1038/ncomms12361, 2016.

Fierce, L., Onasch, T. B., Cappa, C. D., Mazzoleni, C., China, S., Bhandari, J., Davidovits, P., Fischer, D. A., Helgestad, T., Lambe, A. T., Sedlacek, A. J., Smith, G. D., and Wolff, L.: Radiative absorption enhancements by black carbon controlled by particle-to-particle heterogeneity in composition, Proc. Natl. Acad. Sci. U.S.A., 117, 5196–5203, https://doi.org/10.1073/pnas.1919723117, 2020.

Fierce, L., Li, Y., Feng, Y., Riemer, N., Schutgens, N. A. J., Aiken, A. C., Dubey, M. K., Ma, P., and Wuebbles, D.: Constraining Black Carbon Aging in Global Models to Reflect Timescales for Internal Mixing, J Adv Model Earth Syst, 17, https://doi.org/10.1029/2024ms004471, 2025.

Fuller, K. A., Malm, W. C., and Kreidenweis, S. M.: Effects of mixing on extinction by carbonaceous particles, J. Geophys. Res., 104, 15941–15954, https://doi.org/10.1029/1998JD100069, 1999.

Grieshop, A. P., Donahue, N. M., and Robinson, A. L.: Is the gas-particle partitioning in alpha-pinene secondary organic aerosol reversible?, Geophysical Research Letters, 34, 2007GL029987, https://doi.org/10.1029/2007GL029987, 2007.

Habib, Z. G. and Vervisch, P.: On The Refractive Index of Soot at Flame Temperature, Combustion Science and Technology, 59, 261–274, https://doi.org/10.1080/00102208808947100, 1988.

Haywood, J. M. and Shine, K. P.: The effect of anthropogenic sulfate and soot aerosol on the clear sky planetary radiation budget, Geophysical Research Letters, 22, 603–606, https://doi.org/10.1029/95GL00075, 1995.

Healy, R. M., Wang, J. M., Jeong, C. -H., Lee, A. K. Y., Willis, M. D., Jaroudi, E., Zimmerman, N., Hilker, N., Murphy, M., Eckhardt, S., Stohl, A., Abbatt, J. P. D., Wenger, J. C., and Evans, G. J.: Light-absorbing properties of ambient black carbon and brown carbon from fossil fuel and biomass burning sources, JGR Atmospheres, 120, 6619–6633, https://doi.org/10.1002/2015JD023382, 2015.

Heuser, J., Di Biagio, C., Yon, J., Cazaunau, M., Bergé, A., Pangui, E., Zanatta, M., Renzi, L., Marinoni, A., Inomata, S., Yu, C., Bernardoni, V., Chevaillier, S., Ferry, D., Laj, P., Maillé, M., Massabò, D., Mazzei, F., Noyalet, G., Tanimoto, H., Temime-Roussel, B., Vecchi, R., Vernocchi, V., Formenti, P., Picquet-Varrault, B., and Doussin, J.-F.: Spectral optical properties of soot: laboratory investigation of propane flame particles and their link to composition, Atmos. Chem. Phys., 25, 6407–6428, https://doi.org/10.5194/acp-25-6407-2025, 2025.

Huang, X.-F., Peng, Y., Wei, J., Peng, J., Lin, X.-Y., Tang, M.-X., Cheng, Y., Men, Z., Fang, T., Zhang, J., He, L.-Y., Cao, L.-M., Liu, C., Zhang, C., Mao, H., Seinfeld, J. H., and Wang, Y.: Microphysical complexity of black carbon particles restricts their warming potential, One Earth, 7, 136–145, https://doi.org/10.1016/j.oneear.2023.12.004, 2024.

Intergovernmental Panel on Climate Change (IPCC) (Ed.): Short-lived Climate Forcers, in: Climate Change 2021 – The Physical Science Basis: Working Group I Contribution to the Sixth Assessment Report of the Intergovernmental Panel on Climate Change, Cambridge University Press, Cambridge, 817–922, https://doi.org/10.1017/9781009157896.008, 2023.

Kahnert, M. and Devasthale, A.: Black carbon fractal morphology and short-wave radiative impact: a modelling study, Atmos. Chem. Phys., 11, 11745–11759, https://doi.org/10.5194/acp-11-11745-2011, 2011.

Kasper, G.: Dynamics and Measurement of Smokes. I Size Characterization of Nonspherical Particles, Aerosol Science and Technology, 1, 187–199, https://doi.org/10.1080/02786828208958587, 1982.

Kebabian, P. L., Robinson, W. A., and Freedman, A.: Optical extinction monitor using cw cavity enhanced detection, Rev. Sci. Instrum., 78, 063102, https://doi.org/10.1063/1.2744223, 2007.

Khalizov, A. F., Xue, H., Wang, L., Zheng, J., and Zhang, R.: Enhanced Light Absorption and Scattering by Carbon Soot Aerosol Internally Mixed with Sulfuric Acid, J. Phys. Chem. A, 113, 1066–1074, https://doi.org/10.1021/jp807531n, 2009a.

Khalizov, A. F., Zhang, R., Zhang, D., Xue, H., Pagels, J., and McMurry, P. H.: Formation of highly hygroscopic soot aerosols upon internal mixing with sulfuric acid vapor, J. Geophys. Res., 114, 2008JD010595, https://doi.org/10.1029/2008JD010595, 2009b.

Kim, H., Barkey, B., and Paulson, S. E.: Real refractive indices of α- and β-pinene and toluene secondary organic aerosols generated from ozonolysis and photo-oxidation, Journal of Geophysical Research: Atmospheres, 115, https://doi.org/10.1029/2010JD014549, 2010.

Lack, D. A., Cappa, C. D., Cross, E. S., Massoli, P., Ahern, A. T., Davidovits, P., and Onasch, T. B.: Absorption Enhancement of Coated Absorbing Aerosols: Validation of the Photo-Acoustic Technique for Measuring the Enhancement, Aerosol Science and Technology, 43, 1006–1012, https://doi.org/10.1080/02786820903117932, 2009.

Lamkaddam, H., Gratien, A., Pangui, E., Cazaunau, M., Picquet-Varrault, B., and Doussin, J.-F.: High-NOx Photooxidation of n-Dodecane: Temperature Dependence of SOA Formation, Environ. Sci. Technol., 51, 192–201, https://doi.org/10.1021/acs.est.6b03821, 2017.

Lee, D. S., Fahey, D. W., Skowron, A., Allen, M. R., Burkhardt, U., Chen, Q., Doherty, S. J., Freeman, S., Forster, P. M., Fuglestvedt, J., Gettelman, A., De León, R. R., Lim, L. L., Lund, M. T., Millar, R. J., Owen, B., Penner, J. E., Pitari, G., Prather, M. J., Sausen, R., and Wilcox, L. J.: The contribution of global aviation to anthropogenic climate forcing for 2000 to 2018, Atmospheric Environment, 244, 117834, https://doi.org/10.1016/j.atmosenv.2020.117834, 2021.

Lefevre, G., Yon, J., Bouvier, M., Liu, F., and Coppalle, A.: Impact of Organic Coating on Soot Angular and Spectral Scattering Properties, Environ. Sci. Technol., 53, 6383–6391, https://doi.org/10.1021/acs.est.8b05482, 2019.

Liu, D., Allan, J. D., Young, D. E., Coe, H., Beddows, D., Fleming, Z. L., Flynn, M. J., Gallagher, M. W., Harrison, R. M., Lee, J., Prevot, A. S. H., Taylor, J. W., Yin, J., Williams, P. I., and Zotter, P.: Size distribution, mixing state and source apportionment of black carbon aerosol in London during wintertime, Atmos. Chem. Phys., 14, 10061–10084, https://doi.org/10.5194/acp-14-10061-2014, 2014.

Liu, D., Whitehead, J., Alfarra, M. R., Reyes-Villegas, E., Spracklen, D. V., Reddington, C. L., Kong, S., Williams, P. I., Ting, Y.-C., Haslett, S., Taylor, J. W., Flynn, M. J., Morgan, W. T., McFiggans, G., Coe, H., and Allan, J. D.: Black-carbon absorption enhancement in the atmosphere determined by particle mixing state, Nature Geosci, 10, 184–188, https://doi.org/10.1038/ngeo2901, 2017.

Liu, D., He, C., Schwarz, J. P., and Wang, X.: Lifecycle of light-absorbing carbonaceous aerosols in the atmosphere, npj Clim Atmos Sci, 3, 40, https://doi.org/10.1038/s41612-020-00145-8, 2020.

Liu, F., Yon, J., and Bescond, A.: On the radiative properties of soot aggregates – Part 2: Effects of coating, Journal of Quantitative Spectroscopy and Radiative Transfer, 172, 134–145, https://doi.org/10.1016/j.jqsrt.2015.08.005, 2016.

Liu, S., Aiken, A. C., Gorkowski, K., Dubey, M. K., Cappa, C. D., Williams, L. R., Herndon, S. C., Massoli, P., Fortner, E. C., Chhabra, P. S., Brooks, W. A., Onasch, T. B., Jayne, J. T., Worsnop, D. R., China, S., Sharma, N., Mazzoleni, C., Xu, L., Ng, N. L., Liu, D., Allan, J. D., Lee, J. D., Fleming, Z. L., Mohr, C., Zotter, P., Szidat, S., and Prévôt, A. S. H.: Enhanced

light absorption by mixed source black and brown carbon particles in UK winter, Nat Commun, 6, 8435, https://doi.org/10.1038/ncomms9435, 2015.

Maricq, M. M. and Xu, N.: The effective density and fractal dimension of soot particles from premixed flames and motor vehicle exhaust, Journal of Aerosol Science, 35, 1251–1274, https://doi.org/10.1016/j.jaerosci.2004.05.002, 2004.

Massabò, D., Bernardoni, V., Bove, M. C., Brunengo, A., Cuccia, E., Piazzalunga, A., Prati, P., Valli, G., and Vecchi, R.: A multi-wavelength optical set-up for the characterization of carbonaceous particulate matter, Journal of Aerosol Science, 60, 34–46, https://doi.org/10.1016/j.jaerosci.2013.02.006, 2013.

Massoli, P., Murphy, D. M., Lack, D. A., Baynard, T., Brock, C. A., and Lovejoy, E. R.: Uncertainty in Light Scattering Measurements by TSI Nephelometer: Results from Laboratory Studies and Implications for Ambient Measurements, Aerosol Science and Technology, 43, 1064–1074, https://doi.org/10.1080/02786820903156542, 2009.

Massoli, P., Kebabian, P. L., Onasch, T. B., Hills, F. B., and Freedman, A.: Aerosol Light Extinction Measurements by Cavity Attenuated Phase Shift (CAPS) Spectroscopy: Laboratory Validation and Field Deployment of a Compact Aerosol Particle Extinction Monitor, Aerosol Science and Technology, 44, 428–435, https://doi.org/10.1080/02786821003716599, 2010.

McMeeking, G. R., Fortner, E., Onasch, T. B., Taylor, J. W., Flynn, M., Coe, H., and Kreidenweis, S. M.: Impacts of nonrefractory material on light absorption by aerosols emitted from biomass burning, Journal of Geophysical Research: Atmospheres, 119, 12,272-12,286, https://doi.org/10.1002/2014JD021750, 2014.

Metcalf, A. R., Loza, C. L., Coggon, M. M., Craven, J. S., Jonsson, H. H., Flagan, R. C., and Seinfeld, J. H.: Secondary Organic Aerosol Coating Formation and Evaporation: Chamber Studies Using Black Carbon Seed Aerosol and the Single-Particle Soot Photometer, Aerosol Science and Technology, 47, 326–347, https://doi.org/10.1080/02786826.2012.750712, 2013.

Moore, R. H., Ziemba, L. D., Dutcher, D., Beyersdorf, A. J., Chan, K., Crumeyrolle, S., Raymond, T. M., Thornhill, K. L., Winstead, E. L., and Anderson, B. E.: Mapping the Operation of the Miniature Combustion Aerosol Standard (Mini-CAST) Soot Generator, Aerosol Science and Technology, 48, 467–479, https://doi.org/10.1080/02786826.2014.890694, 2014.

Moosmüller, H. and Ogren, J. A.: Parameterization of the Aerosol Upscatter Fraction as Function of the Backscatter Fraction and Their Relationships to the Asymmetry Parameter for Radiative Transfer Calculations, Atmosphere, 8, 133, https://doi.org/10.3390/atmos8080133, 2017.

Onasch, T. B., Massoli, P., Kebabian, P. L., Hills, F. B., Bacon, F. W., and Freedman, A.: Single Scattering Albedo Monitor for Airborne Particulates, Aerosol Science and Technology, 49, 267–279, https://doi.org/10.1080/02786826.2015.1022248, 2015.

Park, K., Cao, F., Kittelson, D. B., and McMurry, P. H.: Relationship between Particle Mass and Mobility for Diesel Exhaust Particles, Environ. Sci. Technol., 37, 577–583, https://doi.org/10.1021/es025960v, 2003.

Peng, J., Hu, M., Guo, S., Du, Z., Zheng, J., Shang, D., Levy Zamora, M., Zeng, L., Shao, M., Wu, Y.-S., Zheng, J., Wang, Y., Glen, C. R., Collins, D. R., Molina, M. J., and Zhang, R.: Markedly enhanced absorption and direct radiative forcing

of black carbon under polluted urban environments, Proc Natl Acad Sci USA, 113, 4266–4271, https://doi.org/10.1073/pnas.1602310113, 2016.

Petzold, A., Schloesser, H., Sheridan, P. J., Arnott, W. P., Ogren, J. A., and Virkkula, A.: Evaluation of Multiangle Absorption Photometry for Measuring Aerosol Light Absorption, Aerosol Science and Technology, 39, 40–51, https://doi.org/10.1080/027868290901945, 2005.

Romshoo, B., Müller, T., Ahlawat, A., Wiedensohler, A., Haneef, M. V., Imran, Mohd., Warsi, A. B., Mandariya, A. K., Habib, G., and Pöhlker, M. L.: Significant contribution of fractal morphology to aerosol light absorption in polluted environments dominated by black carbon (BC), npj Clim Atmos Sci, 7, 87, https://doi.org/10.1038/s41612-024-00634-0, 2024.

Saffaripour, M., Tay, L.-L., Thomson, K. A., Smallwood, G. J., Brem, B. T., Durdina, L., and Johnson, M.: Raman spectroscopy and TEM characterization of solid particulate matter emitted from soot generators and aircraft turbine engines, Aerosol Science and Technology, 51, 518–531, https://doi.org/10.1080/02786826.2016.1274368, 2017.

Sand, M., Samset, B. H., Myhre, G., Gliß, J., Bauer, S. E., Bian, H., Chin, M., Checa-Garcia, R., Ginoux, P., Kipling, Z., Kirkevåg, A., Kokkola, H., Le Sager, P., Lund, M. T., Matsui, H., van Noije, T., Olivié, D. J. L., Remy, S., Schulz, M., Stier, P., Stjern, C. W., Takemura, T., Tsigaridis, K., Tsyro, S. G., and Watson-Parris, D.: Aerosol absorption in global models from AeroCom phase III, Atmospheric Chemistry and Physics, 21, 15929–15947, https://doi.org/10.5194/acp-21-15929-2021, 2021.

Schnaiter, M., Linke, C., Möhler, O., Naumann, K. -H., Saathoff, H., Wagner, R., Schurath, U., and Wehner, B.: Absorption amplification of black carbon internally mixed with secondary organic aerosol, J. Geophys. Res., 110, 2005JD006046, https://doi.org/10.1029/2005JD006046, 2005.

Schwarz, J. P., Gao, R. S., Fahey, D. W., Thomson, D. S., Watts, L. A., Wilson, J. C., Reeves, J. M., Darbeheshti, M., Baumgardner, D. G., Kok, G. L., Chung, S. H., Schulz, M., Hendricks, J., Lauer, A., Kärcher, B., Slowik, J. G., Rosenlof, K. H., Thompson, T. L., Langford, A. O., Loewenstein, M., and Aikin, K. C.: Single-particle measurements of midlatitude black carbon and light-scattering aerosols from the boundary layer to the lower stratosphere, J. Geophys. Res., 111, 2006JD007076, https://doi.org/10.1029/2006JD007076, 2006.

Sedlacek III, A. J., Lewis, E. R., Kleinman, L., Xu, J., and Zhang, Q.: Determination of and evidence for non-core-shell structure of particles containing black carbon using the Single-Particle Soot Photometer (SP2), Geophysical Research Letters, 39, https://doi.org/10.1029/2012GL050905, 2012.

Sorensen, C. M.: The Mobility of Fractal Aggregates: A Review, Aerosol Science and Technology, 45, 765–779, https://doi.org/10.1080/02786826.2011.560909, 2011.

Stephens, M., Turner, N., and Sandberg, J.: Particle identification by laser-induced incandescence in a solid-state laser cavity, Applied Optics, Vol. 42, Issue 19, pp. 3726-3736, https://doi.org/10.1364/AO.42.003726, 2003.

Taylor, J. W., Wu, H., Szpek, K., Bower, K., Crawford, I., Flynn, M. J., Williams, P. I., Dorsey, J., Langridge, J. M., Cotterell, M. I., Fox, C., Davies, N. W., Haywood, J. M., and Coe, H.: Absorption closure in highly aged biomass burning smoke, Atmospheric Chemistry and Physics, 20, 11201–11221, https://doi.org/10.5194/acp-20-11201-2020, 2020.

Vecchi, R., Bernardoni, V., Paganelli, C., and Valli, G.: A filter-based light-absorption measurement with polar photometer: Effects of sampling artefacts from organic carbon, Journal of Aerosol Science, 70, 15–25, https://doi.org/10.1016/j.jaerosci.2013.12.012, 2014.

Wang, J., Doussin, J. F., Perrier, S., Perraudin, E., Katrib, Y., Pangui, E., and Picquet-Varrault, B.: Design of a new multi-phase experimental simulation chamber for atmospheric photosmog, aerosol and cloud chemistry research, Atmos. Meas. Tech., 4, 2465–2494, https://doi.org/10.5194/amt-4-2465-2011, 2011.

Wang, J., Wang, J., Cai, R., Liu, C., Jiang, J., Nie, W., Wang, J., Moteki, N., Zaveri, R. A., Huang, X., Ma, N., Chen, G., Wang, Z., Jin, Y., Cai, J., Zhang, Y., Chi, X., Holanda, B. A., Xing, J., Liu, T., Qi, X., Wang, Q., Pöhlker, C., Su, H., Cheng, Y., Wang, S., Hao, J., Andreae, M. O., and Ding, A.: Unified theoretical framework for black carbon mixing state allows greater accuracy of climate effect estimation, Nat Commun, 14, 2703, https://doi.org/10.1038/s41467-023-38330-x, 2023.

Wang, Y., Liu, F., He, C., Bi, L., Cheng, T., Wang, Z., Zhang, H., Zhang, X., Shi, Z., and Li, W.: Fractal Dimensions and Mixing Structures of Soot Particles during Atmospheric Processing, Environ. Sci. Technol. Lett., 4, 487–493, https://doi.org/10.1021/acs.estlett.7b00418, 2017.

Wu, Y., Cheng, T., Pan, X., Zheng, L., Shi, S., and Liu, H.: The role of biomass burning states in light absorption enhancement of carbonaceous aerosols, Sci Rep, 10, 12829, https://doi.org/10.1038/s41598-020-69611-w, 2020.

Yon, J., Bescond, A., and Ouf, F.-X.: A simple semi-empirical model for effective density measurements of fractal aggregates, Journal of Aerosol Science, 87, 28–37, https://doi.org/10.1016/j.jaerosci.2015.05.003, 2015.

Yu, C., Pangui, E., Tu, K., Cazaunau, M., Feingesicht, M., Xavier, L., Bourrianne, T., Michoud, V., Cantrell, C., Onasch, T. B., Freedman, A., and Formenti, P.: Characterisation of particle single-scattering albedo with a modified airborne dual-wavelength CAPS monitor, Atmospheric Measurement Techniques, 17, 3419–3437, https://doi.org/10.5194/amt-17-3419-2024, 2024.

Zanatta, M., Bogert, P., Ginot, P., Gong, Y., Hoshyaripour, G. A., Hu, Y., Jiang, F., Laj, P., Li, Y., Linke, C., Möhler, O., Saathoff, H., Schnaiter, M., Umo, N. S., Vogel, F., and Wagner, R.: AIDA Arctic transport experiment – Part 1: Simulation of northward transport and aging effect on fundamental black carbon properties, Aerosol Research, 3, 477–502, https://doi.org/10.5194/ar-3-477-2025, 2025.

Zeng, L., Tan, T., Zhao, G., Du, Z., Hu, S., Shang, D., and Hu, M.: Overestimation of black carbon light absorption due to mixing state heterogeneity, npj Clim Atmos Sci, 7, 1–8, https://doi.org/10.1038/s41612-023-00535-8, 2024.

Zhang, R., Khalizov, A. F., Pagels, J., Zhang, D., Xue, H., and McMurry, P. H.: Variability in morphology, hygroscopicity, and optical properties of soot aerosols during atmospheric processing, Proc. Natl. Acad. Sci. U.S.A., 105, 10291–10296, https://doi.org/10.1073/pnas.0804860105, 2008.

Zhang, X., Mao, M., Yin, Y., and Wang, B.: Absorption enhancement of aged black carbon aerosols affected by their microphysics: A numerical investigation, Journal of Quantitative Spectroscopy and Radiative Transfer, 202, 90–97, https://doi.org/10.1016/j.jqsrt.2017.07.025, 2017.

Zhang, Y., Favez, O., Canonaco, F., Liu, D., Močnik, G., Amodeo, T., Sciare, J., Prévôt, A. S. H., Gros, V., and Albinet, A.: Evidence of major secondary organic aerosol contribution to lensing effect black carbon absorption enhancement, npj Clim Atmos Sci, 1, 47, https://doi.org/10.1038/s41612-018-0056-2, 2018.

Zhang, Y., Su, H., Kecorius, S., Ma, N., Wang, Z., Sun, Y., Zhang, Q., Pöschl, U., Wiedensohler, A., Andreae, M. O., and Cheng, Y.: Extremely low-volatility organic coating leads to underestimation of black carbon climate impact, One Earth, 6, 158–166, https://doi.org/10.1016/j.oneear.2023.01.009, 2023.

Zhang, Z., Wang, Y., Chen, X., Xu, L., Zheng, Z., Ching, J., Zhu, S., Liu, D., and Li, W.: Absorption enhancement and shielding effect of brown organic coating on black carbon aerosols, npj Clim Atmos Sci, 8, 102, https://doi.org/10.1038/s41612-025-00989-y, 2025.